Simulation of Multipath Reflections from Planetary Bodies: Theory and Application to the Lunar South Pole

Marc Sanchez Net*

ABSTRACT. — This article describes a new simulation model to estimate multipath reflections from planetary bodies in the solar system for which a digital elevation map (DEM) is available, but its spatial resolution is significantly larger than the carrier wavelength. To account for uncertainty in the terrain roughness within a DEM facet, we assume that its surface can be modeled as a two-dimensional Gaussian random process and derive its radar cross-section (RCS) under the high-frequency approximation (Geometric Optics). Our solution extends the range of validity of these approximations to low-incidence angles, shows that the RCS can be decomposed into a coherent and non-coherent term, and obtains closed-form expressions for polygonal facets with any number of sides.

Once the simulation model has been presented, we apply it to a downlink between a rover on the lunar South Pole and a Deep Space Network (DSN) station. We show that the model produces sensible results, increasing the amount of reflected power when the elevation angle subtended by Earth in the lunar sky decreases. We also show how the model can be coupled with orbital simulators to obtain a full characterization of the multipath environment using the delay and Doppler spread.

I. Introduction

This article presents a new simulation model to estimate the radar cross-section (RCS) of a planetary body for which a digital elevation map (DEM) of its surface is available. It was originally developed to quantify the severity of multipath fading in links between landed assets on the lunar South Pole and Earth. However, it is broadly

*Communications Architectures and Research Section.

The research described in this publication was carried out by the Jet Propulsion Laboratory, California Institute of Technology, under a contract with the National Aeronautics and Space Administration.

applicable to any form of bistatic experiment in which a spacecraft (landed or in orbit) transmits or receives signals reflected from the surface of planetary body.

Understanding the impact of multipath fading is critical for several missions currently being developed at NASA. For instance, the Volatiles Investigating Polar Exploration Rover (VIPER), currently in design phase, considers multipath fading to be one of the primary sources of mission risk. Therefore, the channel models resulting from the presented model will be used to quantify link performance, evaluate the need for contingency operations, and ultimately, test the flight radio in an emulated multipath environment prior to launch. Similarly, the same models will also be used to inform the design of the Human Landing System, which is also expected to land on the lunar South Pole in the coming years.

This article is broadly divided into four parts. First, we discuss how the surface DEM is preprocessed so that it can be efficiently incorporated in our electromagnetic (EM) wave simulation engine. Second, we describe the multipath fading model, including the difference between coherent and non-coherent scattering, as well as models for diffraction and shadowing effects. Third, we describe how the RCS of each facet in the DEM is calculated using the Geometric Optics approximation. And finally, we exemplify the results of the model using a notional lander located close to the lunar South Pole and transmitting to a Deep Space Network (DSN) 34-meter antenna.

II. Preliminaries

This section introduces two topics. First, it summarizes our terrain model, including its specification as an adaptive three-dimensional mesh for which visibility constraints must be efficiently calculated. Second, it introduces the different coordinate reference systems used in this article and explains how to transform between them. Note that none of this material is the main focus of this article. Consequently, the explanation provided is rather superficial and intended to provide just enough context to make the results in Section IV understandable.

A. Terrain Model

We assume that a model of the surface of a planetary body is available in the form of a DEM. This DEM defines a set of projected Cartesian coordinates that map points on the surface (x, y) to altitudes z above the body's reference ellipsoid. These points are spaced uniformly with resolution Δx and Δy, respectively, which depends on the capabilities of the altimeter used to collect the raw data from which the DEM is produced, as well as the extent of the DEM. For instance, Figure 1 plots the terrain altitude of part of the lunar southern hemisphere, extending from latitude $-80°$ to the South Pole, which is situated at coordinates $(0, 0)$. The original data, available at [1], is provided with a resolution of 20 m in both the x and y directions but has been downsampled to 2 km for plotting purposes.

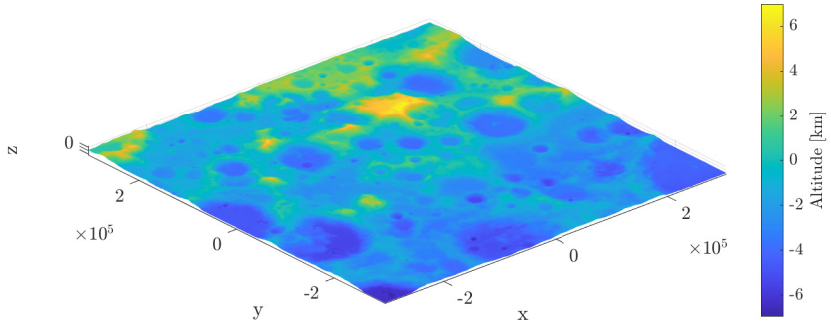

Figure 1. Lunar South Pole DEM

A key question when working with a DEM is whether the available resolution is sufficient to resolve the physical phenomena being studied. In our case, we are interested in understanding reflections of EM waves from the surface, which implies that the DEM resolution must be compared to the wavelength of the signal's carrier frequency. In that sense, an X-band (8.4 GHz) sinusoid has a wavelength of 3.57 cm, which is at least two orders of magnitude smaller than the finest available resolution, 5 m. Therefore, the available lunar DEMs are electrically undersampled and underestimate the roughness properties of the terrain.

To solve this limitation, we propose to use a terrain model that combines the DEM with a stochastic representation of roughness. The basic idea is to partition the surface into a collection of facets that determine the average altitude above the body's reference ellipsoid (see Section II.A.1 for details on how this is accomplished). Then random roughness is added to this average altitude, modeled as a Gaussian stochastic two-dimensional process with zero mean. Note that, implicitly, this assumes the DEM to be error-free and to provide a perfect representation of the average terrain altitude. While this is clearly not possible in real-life, this article we will neglect DEM errors for simplicity.

Using an ideal DEM, we can express the terrain altitude for any given facet as

$$z(x, y) = \bar{z}(x, y) + \zeta(x, y) \tag{1}$$

where $\bar{z}(x, y)$ is the average terrain altitude as provided by points in the DEM, and $\zeta(x, y)$ is a Gaussian process with zero mean and a covariance and autocorrelation matrix that are unknown but can be approximated from the terrain's physical properties. In particular, if we consider the surface to be isotropic, then the covariance matrix is diagonal and defined by a single parameter, the roughness root-mean-squared (rms) height, which we denote by s [2]. Similarly, the autocorrelation function decays as the distance

$$\xi = \sqrt{(x - x')^2 + (y - y')^2} \tag{2}$$

between two points (x, y) and (x', y') increases. Several mathematical functions have been used in the literature to model this decay, including exponential, Gaussian,

Gaussian exponential, and power-law correlation functions [3]. In this article, however, we will mostly restrict our analysis to (normalized) Gaussian correlation functions

$$\rho(\xi) = e^{-\xi^2/l^2}, \tag{3}$$

where l is a characteristic parameter that indicates the distance at which the autocorrelation has decayed to a value of $1/e$. Note that this is consistent with previous works in the literature (e.g., [4, 2]). Note also that some studies have found an exponential autocorrelation to be slightly more realistic in Earth soils [5], but we do not adopt it here due to the fact it is not differentiable at $\xi = 0$, a fact that yields the analytical results later presented intractable.

To illustrate the effect of l on the terrain, Figure 2 plots three randomly generated square surfaces assuming $s = 1$ and l varying from 1 m to 15 m. Note that as l increases, the surface tends to undulate more gently, since points further away are increasingly autocorrelated.

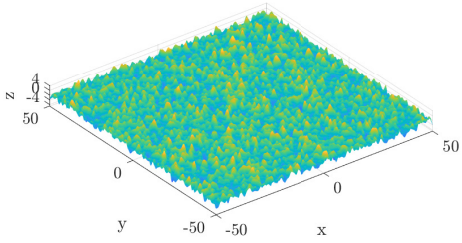

(a) $l = 1$ **m**

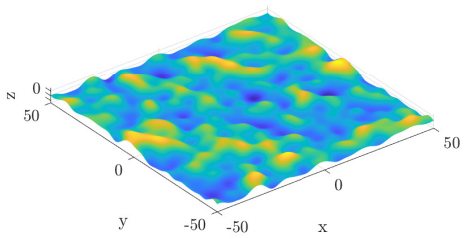

(b) $l = 5$ **m**

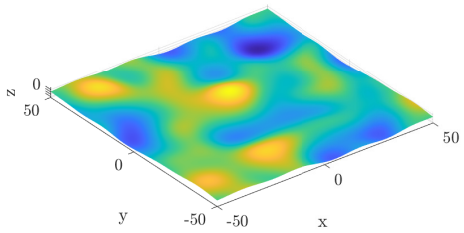

(c) $l = 15$ **m**

Figure 2. Random terrain with $s = 1$ and different correlation lengths

1. Terrain Meshing

Having described the statistical properties of ζ, we now focus our attention on the average altitude $\bar{z}$ from the DEM. In particular, we assume that the discrete points in the DEM can be used as vertices in a three-dimensional mesh of polygons, also known as facets.[1] This mesh is constructed by means of a connectivity matrix with as many

[1] Technically, meshing can be applied to any set of points in any reference frame. Here, we explain the concept assuming that the we are meshing the projected DEM data, but the same concepts apply to all other Cartesian reference systems defined in Section II.B.

rows as polygons in the mesh and as many columns as vertices in a polygon. Each row, therefore, contains a set of numerical indices that identify the points in the DEM to be used as vertices for the facet.

Several methods for triangulation and quadrangulation are available in the literature, and a thorough understanding of how they work is well beyond the scope of this article. In fact, for the purposes of this work, all meshes have been computed using the well-known Delaunay triangulation [6] since it is readily available in MATLAB©. Note that this triangulation is widely used in computational geometry because it tends to avoid sliver triangles, it ensures that each point in the DEM is present at least once in the mesh, and it can be efficiently computed using recursive algorithms.

In Section IV, we show that computing the EM field reflected off of a facet depends on the angle of incidence and reflection of the arriving and departing waves. While these angles are different for each point within a facet, it is common to approximate their value to that of the center of the facet, which we compute as the barycenter of the triangle. However, an additional complication arises when the transmitter (or receiver) is very close to the mesh. In this case, facets close to the transmitter subtend very large solid angles, rendering the barycenter approximation invalid. To solve this problem, we utilize an adaptive meshing algorithm in which facets close the transmitter are subdivided into finer triangles. Importantly, note that no new information about the average height $\bar{z}$ is being added in this process. Indeed, the adaptive meshing algorithm simply uses linear interpolation to create new vertices between the original points in the DEM.

To identify which facets in the original mesh should be subdivided, we approximate the solid angle subtended by a polygon as the ratio between the facet area A_{facet}, and the area of a sphere centered at the transmitter and with radius equal to the distance to the facet's barycenter, denoted d_{facet}. In other words, a facet will be recursively subdivided into smaller facets as long as

$$\frac{A_{\text{facet}}}{4\pi d_{\text{facet}}^2} \leq \varepsilon. \tag{4}$$

Here, ε is a constant that is adjusted so that facets are large enough that they can be considered infinitely large from an electrical perspective. For instance, in our case, ε is calibrated so that no triangle has a side less than 10λ, where λ is the wavelength of the carrier frequency. Also, this method of subdividing the mesh is technically correct only when the terrain is located in the far-field region of the transmitting antenna. Depending on the diameter of the transmit antenna, and the operating frequency, this might not be the case. However, in this article we must assume far-field operation because, otherwise, the equations in Section IV cannot be solved analytically and we would need to resort to numerical integration over the Moon's surface to solve the reflection problem, an approach computationally intractable with regular computers.

To exemplify how the adaptive mesh algorithm works, Figure 3 shows the result of meshing the lunar surface around a landed spacecraft, which we assume to be located

at the Shackleton crater rim (see red dot). As expected, the resulting mesh has varying facet sizes, with smaller triangles just under the landing point. Additionally, the transition regions between different triangle sizes roughly describe circles, which is expected given that we used a sphere to identify facets that need to be subdivided.

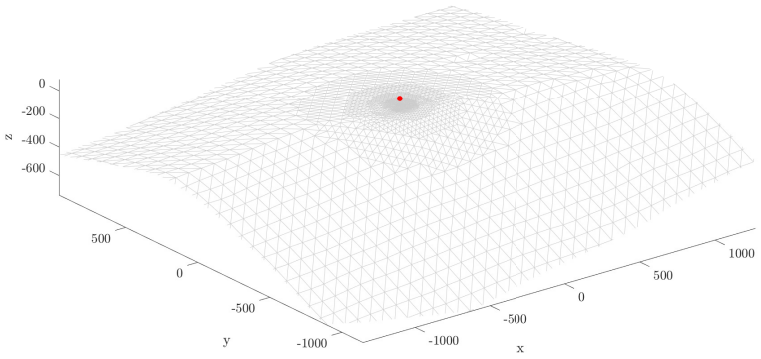

Figure 3. Adaptive Mesh Example

2. Terrain Visibility

Once the terrain has been meshed, we wish to determine which facets are in view of the transmitter and receiver, and thus are candidates for reflecting power. To that end, and following the works of Ulaby et al. [4], we use a simplified single-bounce model that neglects power contributions for double or higher order reflections. This has been found to be a reasonable approximation for modeling similar phenomenal (e.g., radar echos from the ocean waves [7]).

To estimate whether a facet reflects power between the transmitter and receiver, we need to compute whether it is in direct line of sight (LoS) to both of them. Therefore, the problem can be decomposed in three steps: First, determine a boolean index that indicates if a facet is visible from the transmitter. Then repeat the same process but with the receiver. Finally, compute the final visibility mask as the bit-wise *and* boolean operation between the two previously calculated masks.

To estimate whether a facet is visible, we use a set of tools originally developed for computational geometry and ray tracing, most notably the Möller-Trumbore intersection algorithm [8], which provides an efficient procedure to calculate whether a ray, line, or segment intersects with a triangle in three-dimensional space. In that sense, let T denote one of the triangles in the mesh for which we want to calculate the visibility from the transmitter. Then we can use the Möller-Trumbore algorithm to estimate whether a segment delimited by T on one end and the transmitter on the other end, intersects with any triangle other than T in the mesh.

The main drawback of this terrain visibility algorithm is its exponential computational

complexity. Indeed, the worst-case number of operations to determine the visibility of one triangle is $O(F)$, where F is the total number of facets in the mesh. Therefore, the worst-case complexity of the terrain visibility algorithm is $O(F^2)$, resulting in several minutes of computational effort even if the algorithm is parallelized.

To alleviate this problem, we use the well-known method of octrees to recursively subdivide the terrain into octants. Each subdivision is characterized by a bounding box that contains all points in the terrain within that subdivision. Therefore, to estimate whether a triangle is visible or not, we first compute whether the ray departing from the transmitter and arriving to the triangle T intersects with any of the octree's bounding boxes. For each box where an intersection is found, we then use the Möller-Trumbore algorithm to calculate whether the ray intersects with any of the triangles within the box. This results in an approximate computational complexity of $O(F \log F)$, which significantly reduces the computational time as compared to a naif terrain visibility algorithm.

Figure 4 plots the result of running the terrain visibility procedure assuming a lander on the Shackleton crater rim carries an antenna that is placed 50 meters above the surface (see red dot). Points on the surface with direct LoS visibility are highlighted in blue.

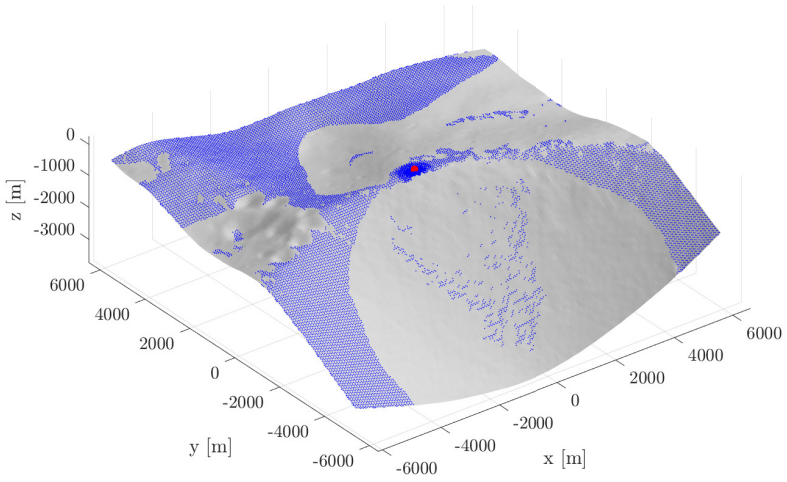

Figure 4. Terrain Visibility Example

B. Coordinate Reference Systems

Up to four different coordinate reference systems (CRSs) are necessary to explain the complete sequence of steps required to estimate the RCS of an arbitrary surface.

1. Projected and Geographic CRS

DEMs are typically provided in a projected coordinate reference system that assigns a set of Cartesian coordinates (x, y, z) to a physical location in a planetary body of

interest. As an example, DEMs of polar regions use a stereographic projection applied to a reference ellipsoid, which can be either a perfect sphere (as is the case for the Moon) or an oblate spheroid (as is the case for Earth).

The physical locations in the projected CRS are transformed to geographic coordinates via a smooth bijective mathematical transformation. Doing so results in a set of spherical coordinates, typically expressed as latitude, longitude, and distance from the center of the planetary body. This geographic CRS is body-fixed (i.e., if the body rotates, so does the frame) and defined such that one axis goes through the axis of rotation, another one lies on the equatorial plane and represents the prime meridian, and the third one completes the right-hand side CRS. Also, transforming latitude, longitude, and distance to equivalent Cartesian coordinates is simply a matter of transforming from spherical to Cartesian coordinates, which is a well-known procedure.

Notwithstanding the complexity of defining and operating with projected and geographic CRSs in planetary bodies, we will assume in this article that software tools such as pyproj [9], MATLAB©, and SPICE [10] can be used to alleviate the effort. Furthermore, while not all bodies in the solar system have well-defined body-fixed CRSs, some of them are standardized by the International Astronomical Unit and are readily available in these tools. This is the case, for instance, of the Moon, for which the standard IAU_MOON CRS has been defined.

2. Antenna and Facet-Local CRS

Once the different locations available in the DEM have been transformed to a geographic CRS and expressed in Cartesian coordinates, it is convenient to perform yet another change of reference frame to operate in an antenna-local reference frame, placed at the transmitting spacecraft. This new CRS is defined as follows:

- The x-axis points from the transmitting spacecraft antenna towards the receiving DSN station. For large distances, however, the exact location of a DSN complex or antenna is not needed, and the center of Earth can be used.
- The z-axis is defined as the cross product between a unitary vector from the center of the planetary body to the location of transmitting antenna (i.e., pointing towards zenith) and the x-axis.
- The y-axis completes the right-hand side CRS and is defined as the cross product between the x-axis and the y-axis.
- The center of the CRS is placed at the transmitting antenna.

Transforming DEM coordinates from a projected CRS to this new antenna-local reference frame is simply a matter of chaining transformations. In other words, we first transform the projected Cartesian coordinates to spherical geographic coordinates. We then transform from geographic spherical coordinates to geographic

Cartesian coordinates. And finally, we transform from geographic Cartesian coordinates to antenna-local Cartesian coordinates using the well-known transformation matrix defined by the three axes previously specified.

Finally, some of the calculations presented later in Section IV can only be analytically performed when working on a facet-local reference frame. Therefore, we now specify how this reference frame is constructed assuming that all terrain coordinates are already expressed in the antenna-local CRS. In this case, we define the facet-local CRS as follows:

- The z-axis is equal to the facet normal.[2]
- The y-axis is defined as the cross product between the z-axis and the direction of incidence of the ray departing from the transmitting antenna towards the facet barycenter.
- The x-axis completes the right-hand side CRS and is defined as the cross product between the y-axis and the z-axis.
- The center of the CRS is placed at the barycenter of the polygonal facet.

Note that, by definition, each facet has its own facet-local CRS. Also, transforming from the antenna-local CRS to the facet-local CRS is immediate and can be achieved using the rotation matrix defined by three unitary vectors previously defined.

III. Multipath Fading Model

This section describes the multipath fading model assumed in this article. To initiate the discussion, let us consider an arbitrary terrain mesh that generates a large number of reflections, one per facet. The total expected scattered power by the surface at any given position in space, can be approximated by adding the power contribution of each individual facet.

Let $\langle P_i \rangle$ denote the expected power scattered by the i-th facet in the terrain.[3] Then, using the bistatic radar Equation [2], we know that

$$\langle P_i \rangle = P_t \frac{G_{t,i} G_{r,i} \lambda^2}{(4\pi)^3 R_{1,i}^2 R_{2,i}^2} \langle \sigma_i \rangle \tag{5}$$

---

[2] While terrain normals can be computed in different ways (e.g., at the center of each facet, at each vertex, etc.), the normal of a polygonal facet has a well-defined unique direction. Furthermore, we assume it always points outward from the planetary body, i.e., in the zenith direction.

[3] In this article, we use $\langle \cdot \rangle$ to denote the sample expectation operator over realizations of the rough terrain surface. This is consistent with previous works in the field (e.g., [4]). However, we acknowledge that other authors use $\langle \cdot \rangle$ to denote expectation over time instead.

where

- P_t is the transmitter power,
- $G_{t,i}$ is the gain of the transmitting antenna over the i-th facet,
- $G_{r,i}$ is the gain of the transmitting antenna over the i-th facet,
- λ is the carrier wavelength,
- $R_{1,i}$ is the distance between the transmitter and the i-th facet barycenter (see Figure 8),
- $R_{2,i}$ is the distance between the i-th facet barycenter and the receiver (see Figure 8),
- $\langle \sigma_i \rangle$ is the expected value for the RCS of the i-th facet in the polarization of the receiving antenna.[4]

Note that, in reality, all these quantities vary within any given facet. However, if the facets are small enough, we can approximate their values as constants and assume that their value can be estimated at each facet's barycenter. Furthermore, note also that the facet RCS is a random variable for which we need to estimate its expected value. Indeed, this follows simply from the fact that the facet RCS depends on the terrain, which has a random roughness component.

In the literature, it is common to decompose the RCS of a facet in its coherent and non-coherent components [4, 7]. This emphasizes the fact that, should you have a perfect description of the average reflecting surface (i.e., you knew $\bar{z}(x, y)$ with perfect precision), you could in theory calculate the reflected power from the coherent reflections using the method from Section III.A. However, from a practical standpoint, it might be more realistic to consider $\langle \sigma_i \rangle$ simply indicative of non-coherent reflected power, especially when operating at large carrier frequencies. Indeed, at centimeter-level wavelengths, errors of the input DEM, the location of the transmit and/or receive antennas, or the location of each facet's electrical center (which technically need not be equal to its barycenter), might be large enough to cause significant phase changes in the reflected fields. These changes, when added together, will result in uniformly distributed random phase variations of the total reflected field, which are akin to the variations resulting from the modeled terrain roughness.

Notwithstanding the challenges associated with modeling the phase of reflected electric fields from the lunar surface, we now proceed to derive the theoretical split between coherently and non-coherently reflected power, assuming no errors or

[4] As shown in Section IV, the proposed model for a facet RCS is polarimetric, i.e., it takes into consideration changes in polarization due to the reflection from the terrain. However, in this section we do not explicitly denote polarization effects to reduce clutter in the equations.

uncertainty other than terrain roughness. In that sense, we first observe that a facet's expected RCS can be estimated as [4]

$$\langle \sigma_i \rangle = 4\pi R_2^2 \frac{\langle |E_{s,i}|^2 \rangle}{|E_i|^2}, \tag{6}$$

where E_i is the amplitude of the incident field at the i-th facet which, again, we assume constant for simplicity. Consequently, we can decompose the facet RCS as follows:

$$\langle \sigma_i \rangle \propto \underbrace{\langle |E_{s,i}| \rangle^2}_{\text{Coherent scattering}} + \underbrace{\text{Var}\{E_{s,i}\}}_{\text{Non-coherent scattering}}. \tag{7}$$

Here, the first term is known as coherent scattering because the resulting electric fields add coherently (i.e., in amplitude and phase). On the other hand, the second term is known as non-coherent scattering because the resulting electric fields have phases that are randomly distributed. Therefore, in general,

$$\langle \sigma_i \rangle = \sigma_i^{coh} + \sigma_i^{ncoh}, \tag{8}$$

where

$$\sigma_i^{coh} = \langle |E_{s,i}| \rangle^2 \tag{9}$$

$$\sigma_i^{ncoh} = \text{Var}\{E_{s,i}\}. \tag{10}$$

and, consequently, we can divide the scattered power contribution of any given facet into two terms:

$$P_i^{coh} = P_t \frac{G_{t,i} G_{r,i} \lambda^2}{(4\pi)^3 R_{1,i}^2 R_{2,i}^2} \sigma_i^{coh} \tag{11}$$

$$P_i^{ncoh} = P_t \frac{G_{t,i} G_{r,i} \lambda^2}{(4\pi)^3 R_{1,i}^2 R_{2,i}^2} \sigma_i^{ncoh} \tag{12}$$

Note that, at this point, this split between coherent and non-coherent power is solely due to terrain roughness. Any other errors in the model, when compared to real life, will likely cause the coherent power term to decrease and the non-coherent power term to increase, up to a point where all reflected power might be considered non-coherent. Ultimately, however, the degree to which a reflection is coherent or non-coherent will need to be ascertained from actual empirical measurements.

A. Coherently Scattered Electric Field

For completeness, we now show how to estimate the phase of the coherent reflected fields from each facet of the DEM. In particular, let us assume that the transmitter sends an ideal unmodulated tone at carrier frequency f_c. In this case, the complex baseband representation of the received signal can be expressed as [11]

$$r_i(t) = C_i e^{-j\phi_i(t)} \tag{13}$$

where

- C_i is the amplitude of the i-th ray and, by definition, is equal to $C_i = \sqrt{P_i^{coh}}$;
- $\phi_i(t)$ is the phase of the i-th ray, which depends on its time delay and Doppler shift.

Furthermore, it is easily shown that the phase of the i-th ray can be expressed as [11]

$$\phi(t) = 2\pi \left[(f_c + f_i)\, \tau_i - f_i t \right] \tag{14}$$

where f_i represents the Doppler shift experienced[5] and τ_i is its propagation delay. Therefore, we can estimate the total coherently scattered electric field as

$$E_s^{coh} = \sum_{i=1}^{F} \sqrt{P_i^{coh}} e^{-j\phi_i(t)} \tag{15}$$

where F is the total number of reflecting facts. Similarly, the total coherently scattered power is

$$P_s^{coh} = \left| E_s^{coh} \right|^2 . \tag{16}$$

B. Non-Coherently Scattered Electric Field

The phase of the non-coherently scattered electric field is assumed to be random and uniformly distributed. This results in

$$E_s^{ncoh} = \sum_{i=1}^{F} \sqrt{P_i^{ncoh}} e^{-j\varphi_i(t)} = \sum_{i=1}^{F} \sqrt{P_i^{ncoh}} \cos\varphi_i + j \sum_{i=1}^{F} \sqrt{P_i^{ncoh}} \sin\varphi_i, \tag{17}$$

where $\varphi_i(t) \sim \text{Uniform}(0, 2\pi)$. Note that both the in-phase and quadrature components of this complex signal are the sum of a large number of these random variables. Therefore, we can invoke the Central Limit Theorem[6] and conclude that

$$E_{sI}^{ncoh} = \sum_{i=1}^{F} \sqrt{P_i^{ncoh}} \cos\varphi_i \sim \mathcal{N}(0, b_0) \tag{18}$$

$$E_{sQ}^{ncoh} = \sum_{i=1}^{F} \sqrt{P_i^{ncoh}} \sin\varphi_i \sim \mathcal{N}(0, b_0) , \tag{19}$$

---

[5] In this paper, we approximate the Doppler shift using the bistatic equation provided in [12], which requires working on a reference frame fixed to the reflection point (i.e., the Moon). Consequently, both the transmitter and receiver have translational velocities due to the relative motion of the Earth and the Moon, as well as any speed imparted by the moving rover. Finally, a third velocity component is generated from the rotation of the transmit and receive antennas around their local azimuth and elevation axis when active tracking is engaged. However, these components are expected to be very small and are thus neglected for simplicity.

[6] Technically, we need to invoke the Lyapunov Central Limit Theorem, which applies to a collection of random variables that are independent but not necessarily identically distributed.

where b_0 denotes the variance of the normal distribution and is equal to

$$2b_0 = \sum_{i=1}^{F} P_i^{ncoh}. \tag{20}$$

Finally, we can combine this result with the coherently scattered electric field to yield

$$E_s = E_s^{coh} + E_s^{ncoh} = E_{sI} + jE_{sQ} \tag{21}$$

with

$$E_{sI} = \Re\{E_s^{coh}\} + E_{sI}^{ncoh} \sim \mathcal{N}(\tilde{\mu}_I, b_0) \tag{22}$$

$$E_{sQ} = \Im\{E_s^{coh}\} + E_{sQ}^{ncoh} \sim \mathcal{N}(\tilde{\mu}_Q, b_0) \tag{23}$$

where $\tilde{\mu}_I$ and $\tilde{\mu}_Q$ are the real and imaginary parts of the total coherently scattered electric field, respectively. Note that, in reality, $\tilde{\mu}_I$, $\tilde{\mu}_Q$, and b_0 are not static parameters and instead vary over time as the Earth-Moon system rotates. However, our notation does not reflect this fact to reduce clutter. Note also that if we accept the premise that all reflected power given by Equation (6) is non-coherent, then

$$\tilde{\mu}_I = 0 \tag{24}$$

$$\tilde{\mu}_Q = 0 \tag{25}$$

$$2b_0 = \frac{P_t \lambda^2}{(4\pi)^3} \sum_{i=1}^{F} \frac{G_{t,i} G_{r,i}}{R_{1,i}^2 R_{2,i}^2} \langle \sigma_i \rangle. \tag{26}$$

C. Rician Multipath Model

In multipath fading models, it is common to assume that there is a direct line of sight ray, as well as reflections from the environment. Let

$$E_{los}(t) = \sqrt{P_{los}} e^{-j\phi_{los}(t)} \tag{27}$$

denote the electric field received from this direct line of sight ray. Then the received total electric field can be estimated as

$$E_{rx} = E_{los} + E_s = E_{rx,I} + jE_{rx,Q} \tag{28}$$

with

$$E_{rx,I} = \Re\{E_{los} + E_s^{coh}\} + E_{sI}^{ncoh} \sim \mathcal{N}(\mu_I, b_0) \tag{29}$$

$$E_{rx,Q} = \Im\{E_{los} + E_s^{coh}\} + E_{sQ}^{ncoh} \sim \mathcal{N}(\mu_Q, b_0). \tag{30}$$

In other words, the average power of the total received field is set by the coherent sum of the LoS ray and the set of coherently scattered rays. Non-coherent scattering, on the other hand, creates random variations around that average power, yielding a total signal envelope that is Rician distributed. In other words,

$$\alpha(t) = |E_{rx}| = \sqrt{|E_{rx,I}|^2 + |E_{rx,Q}|^2} \tag{31}$$

has a probability density function equal to

$$p_\alpha(x) = \frac{2x\,(K+1)}{\Omega_p} \exp\left\{-K - \frac{(K+1)\,x^2}{\Omega_p}\right\} I_0\left(2x\sqrt{\frac{K\,(K+1)}{\Omega_p}}\right) \tag{32}$$

where

$$K = \frac{\mu_I^2 + \mu_Q^2}{2b_0} \tag{33}$$

$$\Omega_p = \mu_I^2 + \mu_Q^2 + 2b_0. \tag{34}$$

In this notation, K is equal to the ratio of coherent vs. non-coherent power, also known as the Rice Factor, while Ω_p is equal to the average envelope power.

To exemplify the behavior of this multipath fading model, consider a lander on the lunar surface trying to communicate with a relay satellite orbiting around the Moon.[7] Figure 5 shows a possible realization of the communication link as the relay satellite rises above the horizon (elevation angle of 0°) and flies over the lander (elevation angle of 90°). It can be clearly observed that at low elevation angles, there is large signal distortion both from the coherent and non-coherent reflection.[8] Furthermore, the sum of the LoS and coherent reflection sets the average received power, while non-coherent scattering causes rapid variations around the mean. Finally, as the satellite increases its elevation with respect to the local terrain, the effects of multipath fading become decreasingly noticeable until, eventually, the received signal varies only due to changes in the free space losses.

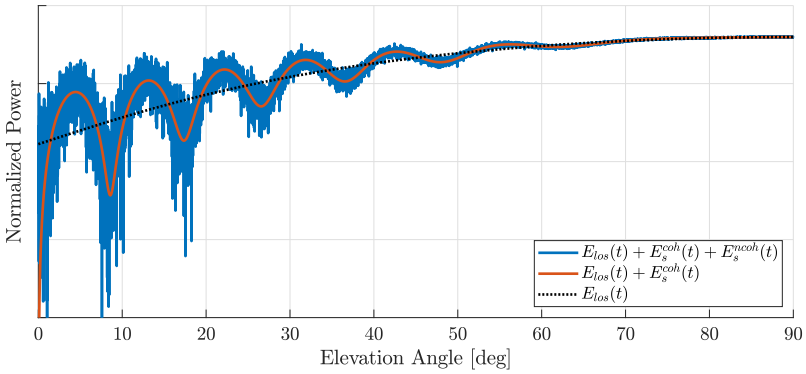

Figure 5. Multipath Fading Model Example

[7] All values in this example are fictional and have been optimized for illustration purposes. They should not be used for decision-making purposes.

[8] It is known that at grazing angles, coherent reflection tends to dominate, a detail obviated here for simplicity.

D. Diffraction

Diffraction refers to physical phenomena that allow EM waves to propagate close to and around obstacles. It can be explained by Huygens's principle, which states that all points on a wavefront can be viewed as point sources of secondary waves [13]. Diffraction effects are particularly noticeable when obstacles block the first Fresnel Zone between a transmitter and receiver [13].

Several models have been developed to account for diffraction loss. The simplest one, known as knife-edge diffraction, is well-known in the literature and models the obstacle as a perfectly opaque half-plane of infinite width. In the context of the Moon, this model has been used to predict the diffraction caused by the lunar limb occulting distant light sources such as stars [14]. Additionally, several studies conducted during the Apollo era considered diffraction from two landed assets by using a solution to the diffraction problem that assumes a perfect sphere [15, 16], which in turn is based on earlier studies for diffraction over convex surfaces [17, 18]. More recently, the development of the Geometric Theory of Diffraction (GTD) and the Unified Theory of Diffraction (UTD) has vastly advanced our ability to understand and model diffraction effects for complex geometries [19, 20].

Notwithstanding the superior performance of UTD to correctly model diffraction effects, we will assume in this article that diffraction can be quantified using classical theory of diffraction over a parabolic cylinder according to the idealized geometry shown in Figure 6. In Figure 6, h_t denotes the altitude of the transmitting antenna

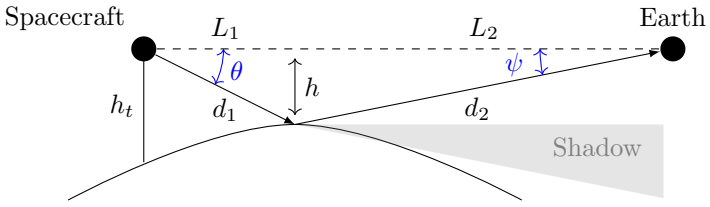

Figure 6. Idealized Diffraction Geometry

above the terrain, h is the clearance distance between the LoS ray and the terrain obstruction,[9] d_1 and d_2 denote the distances from the transmit and receive antennas to the top of the obstruction, L_1 and L_2 represent the projection d_1 and d_2 onto the LoS ray, and θ represents the elevation angle of Earth above the terrain.[10] Using the results from [18], Crysdale showed that the diffraction loss in dB over a cylinder can be approximated as [21]

$$L_D = L_K + L_A, \tag{35}$$

[9] Note that to be consistent with the theory of knife-edge diffraction, h takes negative values when the obstruction does not intersect the LoS ray as shown in Figure 6.

[10] We defined elevation angle as the angular difference between Earth and the surface, as seen from the transmit antenna.

where L_K is the diffraction loss predicted from knife-edge theory. L_A represents an excess loss equal to

$$L_A \approx -20 \log_{10} |1 + m\Psi(m)| . \tag{36}$$

Here, $m = f^{1/3}\psi$, f is the carrier frequency, ψ is defined as in Figure 6, and $\Psi(m)$ is an indefinite integral involving the Airy functions:

$$\Psi(m) = 2j^{-1/3} \int_0^\infty \frac{Ai(u)e^{j^{-1/3}um}}{Ai(u) - jBi(u)} du + 2j \int_0^\infty \frac{Ai(u)e^{jum}}{Ai(u) + jBi(u)} du \tag{37}$$

Fortunately, in the case of $d_2 \gg d_1$, ψ tends to zero and $\tau\Psi(\tau)$ is known to also tend to zero. Consequently, $L_D \approx 0$, so we can approximate the diffraction loss as follows:

$$L_D \approx \frac{1}{2} \left| (\tfrac{1}{2} - C(\nu)) - j(\tfrac{1}{2} - S(\nu)) \right|^2 , \tag{38}$$

where ν is the well-known Fresnel-Kirchhoff parameter

$$\nu = h\sqrt{\frac{2(L_1 + L_2)}{\lambda L_1 L_2}} \approx d_1 \sin\theta \sqrt{\frac{2}{\lambda d_1 \cos\theta}} \approx \sqrt{\frac{2d_1}{\lambda}}\theta, \tag{39}$$

and $C(\nu)$ and $S(\nu)$ denote the complex Fresnel integrals. The first approximation follows from the fact that $L_2 \gg L_1$, while the second one is only applicable when θ is small.

Figure 7 plots the estimated diffraction loss as a function of the elevation angle and the distance d_1 between the transmitting antenna and the ground obstacle for an S-band carrier. As expected, as obstacles get closer, the elevation angle that Earth needs to clear to avoid diffraction losses increases. Alternatively, when the elevation angle is very high, the diffraction loss converges to zero.

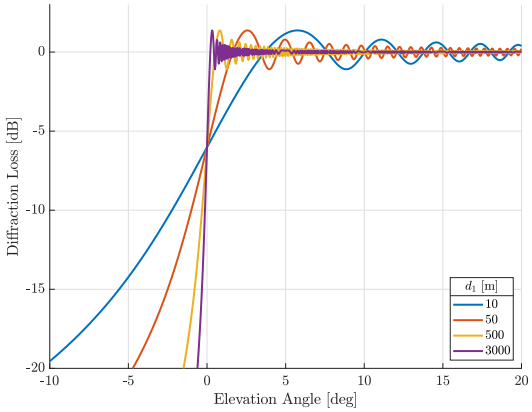

Figure 7. Diffraction Loss

Finally, once the diffraction loss has been calculated, the power received from the direct LoS ray is adjusted as follows:

$$P_{rx} = P_{los} + L_D. \tag{40}$$

Note that in this section we have neglected reflection effects, including any diffraction loss incurred by the multipath rays. We have also simplified the problem by not properly estimating the phase of the diffracted field or depolarization resulting from the diffraction process. Similarly, we have obviated the possibility of multiple diffraction edges, a problem well studied in the literature.

E. Shadowing

Models to calculate the reflected field off of a surface at high incidence angles oftentimes include self-shadowing effects. In essence, these effects model the loss in total received reflected power due impediments caused by the surface roughness. These impediments block scattered rays as they travel from the original reflection point towards the receiver and thus act as natural blockages that reduce the effect of multipath fading.

Modeling of shadowing effects is typically achieved using constants that decrease the terrain RCS [22]:

$$\sigma_w = \sigma S_{in} S_{out}, \tag{41}$$

where σ is the terrain RCS without shadowing, S_{in} captures shadowing of the incident radiation, and S_{out} models shadowing of the scattered radiation. Several options for the values of S_{in} and S_{out} are available in the literature (see [4, 22]) depending on the terrain. Nevertheless, for the purposes of this article, we will ignore shadowing effects. Instead, we rely on the terrain visibility calculations (see section II.A.2) to determine which facets are occulted by the terrain, and ignore the power contributed from those facets. This, in turn, will provide worst-case estimates of the reflected power by the terrain.

IV. Facet Reflection Model

Section III shows that in order to build a multipath fading model, it is necessary to estimate RCS of a rough reflecting surface and separate the coherent and non-coherent scattering components. In this section, we show how to carry such a computation. We note that our analysis is only valid at high carrier frequency (S, X, and Ka-band) and implicitly assumes that the EM wave has infinitesimal small wavelength, at least compared to the terrain features. This simplification, also known as Geometric Optics (GO), allows us to treat the incident and reflected EM waves as rays that are incident onto and reflected by the lunar surface.

To facilitate the analysis, we first consider a simplified scenario in which the facet is horizontally oriented, i.e., it lies in the xy plane, which is defined arbitrarily. Then we show how to modify the obtained results to consider the case of an arbitrarily oriented facet, where the orientation is defined by the facet normal in the antenna-local reference frame as described in Section II.B.2.

Before we proceed with the facet RCS derivations, we note that in this section we use normal font to denote scalar, possibly complex magnitudes. Vectorial magnitudes, on the other hand, are denoted in bold (e.g., a vs. $\boldsymbol{a}$), and unitary vectors are denoted using hat notation (e.g., $\hat{\boldsymbol{a}}$).

A. RCS of a Horizontally-Oriented Rough Facet

Let us consider a single facet that is horizontally oriented (i.e., $\hat{\boldsymbol{z}} = 0$) and assume we are working in its facet-local CRS such that the facet lies in the xy plane. Following the conventions from [4], Figure 8 shows an incident ray on the facet barycenter (in blue) and a scattered ray (in red) towards the receiver.

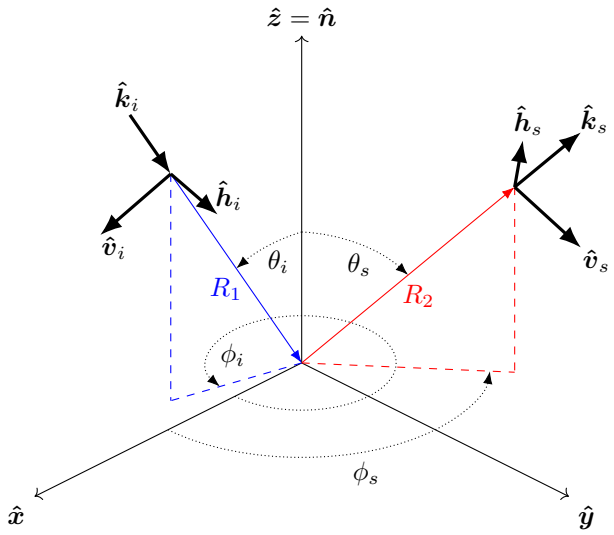

Figure 8. Bistatic Coordinate Reference System with Incident (blue) and Reflected (red) Waves

The different variables required for the analysis of the scattered ray shown in Figure 8 are defined using the Forward Scatter Alignment (FSA) convention:

- $\hat{\boldsymbol{n}}$ denotes the normal to the facet calculated at its barycenter.
- $\hat{\boldsymbol{k}}_i$ and $\hat{\boldsymbol{k}}_s$ denote the unit vectors of incidence and reflection. Because we are assuming planar waves, these vectors also correspond to the direction of propagation of the incident and reflected EM wave.
- $\hat{\boldsymbol{h}}_i$ and $\hat{\boldsymbol{v}}_i$ denote the horizontal and vertical polarization vectors of the incident wave.[11] By the FSA convention, they are defined as $\hat{\boldsymbol{h}}_i = \frac{\hat{\boldsymbol{n}} \times \hat{\boldsymbol{k}}_i}{|\hat{\boldsymbol{n}} \times \hat{\boldsymbol{k}}_i|}$ and $\hat{\boldsymbol{v}}_i = \hat{\boldsymbol{h}}_i \times \hat{\boldsymbol{k}}_i$.

[11] Some references call $\hat{\boldsymbol{h}}$ the perpendicular polarization and $\hat{\boldsymbol{v}}$ the parallel polarization because the $\hat{\boldsymbol{v}}$ always lies in the plane of incidence and $\hat{\boldsymbol{h}}$ is always perpendicular to it.

- $\hat{\boldsymbol{h}}_s$ and $\hat{\boldsymbol{v}}_s$ denote the horizontal and vertical polarization vectors of the reflected wave. By the FSA convention, they are defined as $\hat{\boldsymbol{h}}_s = \frac{\hat{\boldsymbol{n}} \times \hat{\boldsymbol{k}}_s}{|\hat{\boldsymbol{n}} \times \hat{\boldsymbol{k}}_s|}$ and $\hat{\boldsymbol{v}}_s = \hat{\boldsymbol{h}}_s \times \hat{\boldsymbol{k}}_s$.
- θ_i and θ_s are the polar angles of the incident and reflected waves.
- ϕ_i and ϕ_s are the azimuthal angles of the incident and reflected waves.
- R_1 and R_2 denote the distance from the transmitter to the surface (more precisely, the facet's barycenter) and from the surface to the receiver.

To determine the reflected EM field from the incident field, we start our discussion from the Stratton-Chu Equation [4]. It states that under the far field approximation, the scattered field can be estimated by solving the following integral equation:

$$\mathbf{E}_s = \frac{-jk}{4\pi R_2} e^{-jkR_2} \hat{\boldsymbol{k}}_s \times \iint_F \left[\hat{\boldsymbol{n}} \times \mathbf{E}_f - \eta_s \hat{\boldsymbol{k}}_s \times (\hat{\boldsymbol{n}} \times \mathbf{H}_f) \right] e^{jk\hat{\boldsymbol{r}} \cdot \hat{\boldsymbol{k}}_s} dS, \tag{42}$$

where $\mathbf{E}_f$ and $\mathbf{H}_f$ denote the electric and magnetic fields *on* the facet F, η_s is the intrinsic impedance of the medium in which $\mathbf{E}_s$ is scattered,[12] k is the wavenumber of the scattering medium, $\boldsymbol{r}$ is the position of a point in the facet, and the symbol F on the integral limits is used to denote that we are summing over the entire facet. A full derivation of this equation can be found in [4], Appendix 12J, or in [22], Appendix A. Also, we note that Equation (42) is only valid in the far-field (see Appendix I) and that, for the rest of this article, we will assume the incident and scattering medium to be free space so that $k = \frac{2\pi}{\lambda}$ (see Appendix II).

Note that Equation (42) is particularly difficult to solve analytically because the independent variable that we are trying to isolate, i.e., scattered field $\mathbf{E}_s$, appears on both sides of Equation (42). Indeed, the surface field $\mathbf{E}_f$ is the superposition of the incident field $\mathbf{E}_i$ and the scattered field $\mathbf{E}_s$ on the surface. Therefore, without any simplifications, Equation (42) can only be solved numerically.

1. Planar Wave Approximation

Because we are interested in estimating the scattered reflected field at large distances, we can start simplifying the problem by assuming that both the incident and scattered waves are planar. Under this assumption, the incident wave can be expressed as [13]

$$\mathbf{E}_i = E_0 \hat{\boldsymbol{a}} e^{-jk\hat{\boldsymbol{k}}_i \cdot \boldsymbol{r}}. \tag{43}$$

Here, E_0 is the amplitude of the wave at the point of scattering, and $\hat{\boldsymbol{a}}$ is the unitary incident wave polarization vector that can be written as

$$\hat{\boldsymbol{a}} = \left(\alpha_h \hat{\boldsymbol{h}}_i + \alpha_v \hat{\boldsymbol{v}}_i \right), \tag{44}$$

---

[12] η_s equals η_1, the vacuum impedance, when calculating the reflected wave. Alternatively, η_s equals η_2, the impedance of the terrain, when estimating the transmitted wave.

[13] All EM fields in this article obviate the time harmonic term $e^{j\omega t}$ for simplicity. Therefore, they are assumed to be complex magnitudes.

where α_h and α_v are the normalized incident wave polarization coefficients. Note that any desired polarization can be recovered by simply adjusting the values of α_h and α_v. For instance, a vertically polarized wave is obtained by letting $\alpha_h = 0$ and $\alpha_v = 1$, while a right-hand side polarized wave is obtained when $\alpha_h = \frac{1}{\sqrt{2}}$ and $\alpha_v = \frac{j}{\sqrt{2}}$.

2. Tangent-Plane Approximation

Next, let us assume that an approximate solution to Equation (42) can be obtained by the using tangent-plane approximation (also known as Kirchhoff approximation), which states that the total field on the surface is equal to the incident field plus the reflected field by an infinite tangent plane at the point of reflection [4].[14] In other words,

$$\mathbf{E}_f(\boldsymbol{r}) = \mathbf{E}_i(\boldsymbol{r}) + \mathbf{E}_s(\boldsymbol{r}), \tag{45}$$

where $\boldsymbol{r}$ denotes a point on the surface and $\mathbf{E}_s(\boldsymbol{r})$ can be computed using the theory of oblique incidence. After some algebraic manipulation, omitted here for brevity and available in [4], pp. 927-928, it can be shown that this approximation leads to

$$\hat{\boldsymbol{n}} \times \mathbf{E}_f = \left[(1 + R_\perp) \left(\hat{\boldsymbol{a}} \cdot \hat{\boldsymbol{t}} \right) \left(\hat{\boldsymbol{n}} \times \hat{\boldsymbol{t}} \right) - \left(1 - R_\parallel \right) \left(\hat{\boldsymbol{n}} \cdot \hat{\boldsymbol{k}}_i \right) \left(\hat{\boldsymbol{a}} \cdot \hat{\boldsymbol{d}} \right) \hat{\boldsymbol{t}} \right] E_0 e^{-jk\hat{\boldsymbol{k}}_i \cdot \boldsymbol{r}} \tag{46}$$

$$\hat{\boldsymbol{n}} \times \mathbf{H}_f = - \left[(1 - R_\perp) \left(\hat{\boldsymbol{n}} \cdot \hat{\boldsymbol{k}}_i \right) \left(\hat{\boldsymbol{a}} \cdot \hat{\boldsymbol{t}} \right) \hat{\boldsymbol{t}} + \left(1 + R_\parallel \right) \left(\hat{\boldsymbol{a}} \cdot \hat{\boldsymbol{d}} \right) \left(\hat{\boldsymbol{n}} \times \hat{\boldsymbol{t}} \right) \right] \frac{E_0}{\eta_1} e^{-jk\hat{\boldsymbol{k}}_i \cdot \boldsymbol{r}}, \tag{47}$$

where $\left(\hat{\boldsymbol{k}}_i, \hat{\boldsymbol{t}}, \hat{\boldsymbol{d}} \right)$ form a right-hand side coordinate system at the point of reflection such that $\hat{\boldsymbol{t}} = \frac{\hat{\boldsymbol{k}}_i \times \hat{\boldsymbol{n}}}{\left| \hat{\boldsymbol{k}}_i \times \hat{\boldsymbol{n}} \right|}$ is tangential to the surface and $\hat{\boldsymbol{d}} = \hat{\boldsymbol{k}}_i \times \hat{\boldsymbol{t}}$ completes the right-hand CRS. Furthermore, $R_\perp$ and $R_\parallel$ are the Fresnel reflection coefficients for the horizontal and vertical polarization, respectively, calculated as follows:

$$R_\parallel = + \frac{\eta_2 \cos\theta_t - \eta_1 \cos\theta_i}{\eta_2 \cos\theta_t + \eta_1 \cos\theta_i} \tag{48}$$

$$R_\perp = - \frac{\eta_2 \cos\theta_i - \eta_1 \cos\theta_t}{\eta_2 \cos\theta_i + \eta_1 \cos\theta_t}, \tag{49}$$

where θ_i is the polar angle of incidence, θ_t is the polar angle of transmission, and η_1 and η_2 are the intrinsic impedance of the vacuum and the terrain, respectively. Also, θ_i can be calculated by solving Snell's law

$$\varepsilon_1 \sin\theta_i = \varepsilon_2 \sin\theta_t, \tag{50}$$

with $\varepsilon_1 = 1$, the relative permittivity of the vacuum, and ε_2 equal to the possibly complex relative permittivity of the planetary body of interest.[15] Note that if ε_2 is

---

[14] Some authors consider that the surface fields $\mathbf{E}_f$ and $\mathbf{H}_f$ should only be equal to the reflected fields by an infinite tangent plane and neglect the incident field (see, for instance, [7]). For a brief discussion on the choice of surface fields, see [3], section 2.4.3.2.

[15] In this article, we assume that the planetary body has a single layer of soil with homogeneous dielectric properties. In practice, this is a good approximation when the depth of this homogeneous layer of regolith is on the order of the carrier wavelength, which is very short at high frequencies (tens of centimeters at most).

complex, the transmission angle θ_t will also be a complex number. This provides the necessary phase matching at the facet interface so that the boundary conditions between the vacuum and the terrain are satisfied [2]. Note also that substituting Equations (46) and (47) into Equation (42) yields a result in which $\mathbf{E}_s$ no longer appears on both sides of (42), so we have indeed simplified the Stratton-Chu equation. However, it unfortunately remains too complicated to solve analytically, so further approximations are required.

3. Stationary-Phase Approximation

Several approaches to further simplify Equation (42) are available in the literature. They are known as the Small Perturbation Model (SPM), the GO model, and the Physical Optics (PO) model [4, 22]. Their range of validity has been studied in depth in the literature (see, for instance, [22]) and depends on how rough the surface is compared to the carrier wavelength. Additionally, extensions to bridge the SPM, GO, and PO models into a unified theory of reflection are now available in what is known as the Integral Equation Model and its variants [2, 22].

For the purposes of this article, however, we will focus only on the GO model, also known as the stationary-phase approximation. The rationale behind this choice is twofold: first, it is conceptually easy to understand and numerically efficient to implement; and second, it is applicable at the range of frequencies of interest (X-band, Ka-band, even S-band in some cases), where the wavelength is very short, and thus, from an electrical standpoint, the surface undulations can be considered smooth. Note, however, that the classical GO model presented by Ulaby et al. in [4] and adopted by many authors is not applicable at high incidence and reflection angles. Therefore, in what follows we extend the theoretical results so that reflection at grazing angles is well characterized.

The basic principle of the GO model is simple: Consider EM waves as rays of infinite frequency (or zero wavelength) that can only reflect specularly off of a surface. Consequently, any power received at an antenna from a rough surface will arrive from terrain corners for which the conditions of specular reflection are valid (thus neglecting other effects such as diffraction). To express this notion mathematically while simplifying the notation, let us express Equations (46) and (47) as

$$\hat{\boldsymbol{n}} \times \mathbf{E}_f = \boldsymbol{w}_e E_0 e^{-jk\hat{\boldsymbol{k}}_i \cdot \boldsymbol{r}} \tag{51}$$

$$\hat{\boldsymbol{n}} \times \mathbf{H}_f = \boldsymbol{w}_h \frac{E_0}{\eta_1} e^{-jk\hat{\boldsymbol{k}}_i \cdot \boldsymbol{r}}, \tag{52}$$

where $\boldsymbol{w}_e$ and $\boldsymbol{w}_h$ are the vectors resulting from performing all dot and cross-product operations. Now, the Stratton-Chu integral equation can be rewritten as

$$\mathbf{E}_s = \frac{-jk}{4\pi R_2} e^{-jkR_2} E_0 \hat{\boldsymbol{k}}_s \times \iint_F \left[\boldsymbol{w}_e - \hat{\boldsymbol{k}}_s \times \boldsymbol{w}_h \right] e^{j\boldsymbol{q}\cdot\boldsymbol{r}} dS, \tag{53}$$

with

$$\boldsymbol{q} = k\left(\hat{\boldsymbol{k}}_s - \hat{\boldsymbol{k}}_i\right). \tag{54}$$

Furthermore, the condition that only specular reflection contributes to reflected power can be encoded mathematically by having a constant phase on the integrand of Equation (53). To see that this is the case, let a point on the surface have coordinates $\boldsymbol{r} = [x, y, z(x,y)]^T$ so that

$$Q = \boldsymbol{q} \cdot \boldsymbol{r} = q_x x + q_y y + q_z z(x,y). \tag{55}$$

Then, the phase is said to be stationary if

$$\frac{\partial Q}{\partial x} = q_x + q_z \frac{\partial z}{\partial x} = 0 \tag{56}$$

$$\frac{\partial Q}{\partial y} = q_y + q_z \frac{\partial z}{\partial y} = 0, \tag{57}$$

where $\frac{\partial z}{\partial x}$ and $\frac{\partial z}{\partial y}$ denote the surface slopes at the point of interest and they are non-zero because we have assumed a rough surface (i.e., in this section, $\frac{\partial \bar{z}}{\partial x} = \frac{\partial \bar{z}}{\partial y} = 0$ but $\frac{\partial \zeta}{\partial x} \neq 0$ and $\frac{\partial \zeta}{\partial y} \neq 0$). Rearranging the terms in these equations yields

$$\frac{\partial z}{\partial x} = -\frac{q_x}{q_z} \tag{58}$$

$$\frac{\partial z}{\partial y} = -\frac{q_x}{q_z}. \tag{59}$$

Consequently, the local normal at a point of reflection must be equal to [16]

$$\begin{aligned} \hat{\boldsymbol{n}}_{GO} =& \frac{\frac{\partial \boldsymbol{r}}{\partial x} \times \frac{\partial \boldsymbol{r}}{\partial y}}{\left|\frac{\partial \boldsymbol{r}}{\partial x} \times \frac{\partial \boldsymbol{r}}{\partial y}\right|} = \frac{-\frac{\partial z}{\partial x}\hat{\boldsymbol{x}} - \frac{\partial z}{\partial y}\hat{\boldsymbol{y}} + \frac{\partial z}{\partial z}\hat{\boldsymbol{z}}}{\sqrt{\left(\frac{\partial z}{\partial x}\right)^2 + \left(\frac{\partial z}{\partial y}\right)^2 + \left(\frac{\partial z}{\partial z}\right)^2}} = \\ =& \frac{q_x\hat{\boldsymbol{x}} + q_y\hat{\boldsymbol{y}} + q_z\hat{\boldsymbol{z}}}{q_z\sqrt{\left(\frac{q_x}{q_z}\right)^2 + \left(\frac{q_y}{q_z}\right)^2 + 1}} = \frac{\hat{\boldsymbol{k}}_s - \hat{\boldsymbol{k}}_i}{\left|\hat{\boldsymbol{k}}_s - \hat{\boldsymbol{k}}_i\right|}. \end{aligned} \tag{60}$$

Note that except for the trivial case where the surface is perfectly flat, $\hat{\boldsymbol{n}}_{GO}$ is in general not equal to the facet normal $\hat{\boldsymbol{n}}$. Indeed, $\hat{\boldsymbol{n}}$ represents the normal of the average height of the facet $\bar{z}$, assumed to be zero in this section (hence $\hat{\boldsymbol{n}} = \hat{\boldsymbol{z}}$). Alternatively, $\hat{\boldsymbol{n}}_{GO}$ is the normal of a specific set of points within the rough facet for which the terrain slopes orient the surface just in the right way for the conditions of specular reflection to be satisfied.

Next, we assume that the facet is small enough so that the incidence and reflection angles at any point on the facet can be approximated by those calculated from its barycenter. Consequently, for any given facet, the vectors $\boldsymbol{q}$ and $\hat{\boldsymbol{n}}_{GO}$ will be constant

[16] Appendix IV proves that the conditions for specular reflection between the incident and reflected rays are always satisfied with $\hat{\boldsymbol{n}}_{GO}$ defined as in Equation (60).

and, by extension, so will the vectors $\boldsymbol{w}_e$ and $\boldsymbol{w}_h$. As a result, the Stratton-Chu equation simplifies to

$$\mathbf{E}_s = \frac{-jk}{4\pi R_2} e^{-jkR_2} E_0 \left[\hat{\boldsymbol{k}}_s \times \left(\boldsymbol{w}_e - \hat{\boldsymbol{k}}_s \times \boldsymbol{w}_h\right)\right] \iint_F e^{j\boldsymbol{q}\cdot\boldsymbol{r}} dS. \tag{61}$$

In other words, we have shown that for any given facet, the scattered field under the Kirchhoff and GO approximation can be written as

$$\mathbf{E}_s = KE_0 I\boldsymbol{p}, \tag{62}$$

where

$$K = \frac{-jk}{4\pi R_2} e^{-jkR_2} \tag{63}$$

$$I = \iint_F e^{j\boldsymbol{q}\cdot\boldsymbol{r}} dS \tag{64}$$

$$\boldsymbol{p} = \hat{\boldsymbol{k}}_s \times \left(\boldsymbol{w}_e - \hat{\boldsymbol{k}}_s \times \boldsymbol{w}_h\right). \tag{65}$$

Finally, observe that the polarization of the scattered wave will be defined by $\boldsymbol{p}$, the only vectorial magnitude in Equation (62). Therefore, if we want to express $\mathbf{E}_s$ with respect to the scattered polarization vectors $\hat{\boldsymbol{h}}_s$ and $\hat{\boldsymbol{v}}_s$, all we need to do is decompose $\boldsymbol{p}$ into this basis. This step follows with minimal manipulation from previous results by Ulaby et al. ([4], pp. 930-931) and results in

$$\boldsymbol{p} = \left[\left(\alpha_h U_{hh} + \alpha_v U_{hv}\right)\hat{\boldsymbol{h}}_s + \left(\alpha_h U_{hv} + \alpha_v U_{vv}\right)\hat{\boldsymbol{v}}_s\right], \tag{66}$$

where

$$U_{hh} = \chi\left[R_\parallel \left(\hat{\boldsymbol{h}}_s \cdot \hat{\boldsymbol{k}}_i\right)\left(\hat{\boldsymbol{h}}_i \cdot \hat{\boldsymbol{k}}_s\right) + R_\perp \left(\hat{\boldsymbol{v}}_s \cdot \hat{\boldsymbol{k}}_i\right)\left(\hat{\boldsymbol{v}}_i \cdot \hat{\boldsymbol{k}}_s\right)\right] \tag{67}$$

$$U_{hv} = \chi\left[R_\parallel \left(\hat{\boldsymbol{h}}_s \cdot \hat{\boldsymbol{k}}_i\right)\left(\hat{\boldsymbol{v}}_i \cdot \hat{\boldsymbol{k}}_s\right) - R_\perp \left(\hat{\boldsymbol{v}}_s \cdot \hat{\boldsymbol{k}}_i\right)\left(\hat{\boldsymbol{h}}_i \cdot \hat{\boldsymbol{k}}_s\right)\right] \tag{68}$$

$$U_{vh} = \chi\left[R_\parallel \left(\hat{\boldsymbol{v}}_s \cdot \hat{\boldsymbol{k}}_i\right)\left(\hat{\boldsymbol{h}}_i \cdot \hat{\boldsymbol{k}}_s\right) - R_\perp \left(\hat{\boldsymbol{h}}_s \cdot \hat{\boldsymbol{k}}_i\right)\left(\hat{\boldsymbol{v}}_i \cdot \hat{\boldsymbol{k}}_s\right)\right] \tag{69}$$

$$U_{vv} = \chi\left[R_\parallel \left(\hat{\boldsymbol{v}}_s \cdot \hat{\boldsymbol{k}}_i\right)\left(\hat{\boldsymbol{v}}_i \cdot \hat{\boldsymbol{k}}_s\right) + R_\perp \left(\hat{\boldsymbol{h}}_s \cdot \hat{\boldsymbol{k}}_i\right)\left(\hat{\boldsymbol{h}}_i \cdot \hat{\boldsymbol{k}}_s\right)\right], \tag{70}$$

and

$$\chi = \frac{2k\left(1 - \hat{\boldsymbol{k}}_i \cdot \hat{\boldsymbol{k}}_s\right)}{\left(\hat{\boldsymbol{k}}_i \cdot \hat{\boldsymbol{h}}_s\right)^2 + \left(\hat{\boldsymbol{k}}_i \cdot \hat{\boldsymbol{v}}_s\right)^2}. \tag{71}$$

Note that the definition of the normalized polarization coefficients for the transmitted wave, α_h and α_v, is still consistent with Equation (44). Also, $R_\parallel$ and $R_\perp$ are the parallel and perpendicular reflection coefficients from Equations (48) and (49), respectively.

4. Received Electric Field

To calculate the received electric field, we first need to model how the receiving antenna will amplify or attenuate the incoming electric field. In general, this can be

achieved by first modeling (or measuring) the radiation pattern of the receiving antenna in two orthogonal polarizations (typically called co- and cross-polarization) and then assuming the scattered field is passed through two independent polarizers with amplitude equal to the square root of the antenna gain.[17]

Using Jones calculus, we define a polarizer using a two-dimensional matrix of the form

$$\mathbf{P} = \begin{bmatrix} p_{11} & p_{12} \\ p_{21} & p_{22} \end{bmatrix}, \tag{72}$$

where the first dimension corresponds to $\hat{\boldsymbol{h}}_s$ and the second dimension corresponds to $\hat{\boldsymbol{v}}_s$.[18] Consequently, the total received electric field can be expressed as the weighted sum of the cross and co-polarizations:

$$\mathbf{E}_r = \left(\sqrt{G_{co}}\mathbf{P}_{co} + \sqrt{G_{cx}}\mathbf{P}_{cx}\right)\mathbf{E}_s = KE_0 I\left(\sqrt{G_{co}}\mathbf{P}_{co} + \sqrt{G_{cx}}\mathbf{P}_{cx}\right)\boldsymbol{e}, \tag{73}$$

with

$$\boldsymbol{e} = \begin{bmatrix} e_h \\ e_v \end{bmatrix} = \begin{bmatrix} \alpha_h U_{hh} + \alpha_v U_{hv} \\ \alpha_h U_{vh} + \alpha_v U_{vv} \end{bmatrix} \tag{74}$$

and $\mathbf{P}_{co}$ and $\mathbf{P}_{cx}$ representing the co and cross-polarizers of the receiving antenna.

Further simplifications are possible if we assume that the receiving antenna has a high enough cross-polarization rejection level that it can be considered infinite. In that case, $G_{cx} \approx 0$ and, consequently,

$$\mathbf{E}_r = KE_0 I\sqrt{G_{co}}\left[\left(p_{11}^{co}e_h + p_{12}^{co}e_v\right)\hat{\boldsymbol{h}}_s + \left(p_{21}^{co}e_h + p_{22}^{co}e_v\right)\hat{\boldsymbol{v}}_s\right]. \tag{75}$$

5. Facet RCS

Next, we consider how to estimate the RCS σ of a facet based on the received electric field. In particular, if we assume that the receiving antenna fully attenuates the cross-polarization, then

$$\sigma = 4\pi R_2^2 \frac{|\mathbf{E}_r|^2}{G_{co}|E_0|^2}, \tag{76}$$

where we have introduced the term G_{co} so that facet RCS is normalized from the transmit power and gain,[19] as well as the receive antenna gain. Consequently,

$$\begin{aligned} \sigma =& 4\pi R_2^2 \frac{|K|^2 |E_0|^2 |I|^2}{|E_0|^2}\left[|p_{11}e_h + p_{12}e_v|^2 + |p_{21}e_h + p_{22}e_v|^2\right] \\ =& \frac{k^2}{4\pi}|I|^2\left[|p_{11}e_h + p_{12}e_v|^2 + |p_{21}e_h + p_{22}e_v|^2\right]. \end{aligned} \tag{77}$$

---

[17] Our model assumes the polarizers at the receiving antenna do not introduce any relative phase between the two polarizations.

[18] For instance, a right-hand side circular polarizer is modeled as $\mathbf{P} = \frac{1}{2}\begin{bmatrix} 1 & -j \\ j & 1 \end{bmatrix}$.

[19] Recall here that $|E_0|^2$ is proportional to the transmit power and transmit antenna gain.

A similar equation can be derived if both the cross and co-polarization are considered, a step obviated here for brevity. Also, all the parameters in this equation are known except for $|I|^2$. Therefore, we now focus our attention on this term and derive analytical solutions for its value assuming polygonal facets, a random rough surface, and low incidence and reflection angles.

6. The Surface Differential

We wish to evaluate the squared norm of the phase integral [20]

$$I = \iint_F e^{j\boldsymbol{q}\cdot\boldsymbol{r}} dS. \tag{78}$$

By definition,

$$|I|^2 = II^* = \iint_F e^{j\boldsymbol{q}\cdot\boldsymbol{r}} dS \iint_{F'} e^{-j\boldsymbol{q}\cdot\boldsymbol{r'}} dS' = \iint_F \iint_{F'} e^{j\boldsymbol{q}(\boldsymbol{r}-\boldsymbol{r'})} dS dS' \tag{79}$$

and, therefore, we need to evaluate the surface differential dS to be able to estimate its value. In general, it is known that for an arbitrary surface $z(x, y)$,

$$dS = \sqrt{\left(\frac{\partial z}{\partial x}\right)^2 + \left(\frac{\partial z}{\partial y}\right)^2 + \left(\frac{\partial z}{\partial z}\right)^2}\, dA, \tag{80}$$

which clearly indicates that the constant relating the surface differential dS with the area differential $dA = dxdy$ depends on the slopes of the surface over the region of integration. In our case, however, these slopes are random variables because the surface itself is treated as a random variable. To circumvent this problem, three approximations are possible:

- first, from Equations (58) and (59), we get $dS_1 \approx \frac{q}{|q_z|} dA$ (see also [4], p. 933);
- second, if we assume that the slopes are small, then $\left(\frac{\partial z}{\partial x}\right)^2 \ll 1$ and $\left(\frac{\partial z}{\partial y}\right)^2 \ll 1$ and, therefore, $dS_2 \approx dA$;
- and third, if we assume that the surface slopes are uncorrelated with the terrain altitude, then we show in Appendix V that $dS_3 \approx \sqrt{1 + \frac{4s^2}{l^2}} dA$, where s and l are the surface roughness and correlation length as defined in Section II.A.

Observe that dS_1 can be problematic when evaluating reflections at grazing angles. Indeed, under these conditions, q_z tends to 0 and therefore the surface differential tends to infinity, a condition that makes no physical sense because it might cause facets to reflect more power than the amount of power incident on them. On the other hand, dS_2 tends to underestimate the correction factor relating dA and dS as it

[20] Some authors indicate the RCS of a surface is proportional to its Fourier transform. Indeed, Equation (78) can be viewed as a two-dimensional Fourier transform of a mask having ones in the surface extent and zeros elsewhere.

assumes that the slopes are very small, a condition not necessarily true in our analysis. Therefore, for the rest of the discussion, we will assume that

$$dS = \sqrt{1 + \tfrac{4s^2}{l^2}} dA, \tag{81}$$

a condition that relates the dS and dA by the average slope of the surface given its statistical roughness characteristics.

7. Phase Integral

We now proceed with the derivation of $|I|^2$. In particular, we note that

$$\boldsymbol{q}\,(\boldsymbol{r} - \boldsymbol{r'}) = q_x(x - x') + q_y(y - y') + q_z(z - z') \tag{82}$$

where, by construction, z and z' are random variables as in Equation (1). Therefore, $|I|^2$ is also a random variable and we seek its expected value:

$$\langle |I|^2 \rangle = \langle \iint_F \iint_{F'} e^{j\boldsymbol{q}(\boldsymbol{r}-\boldsymbol{r'})} dS dS' \rangle. \tag{83}$$

To derive a closed-form solution for $\langle |I|^2 \rangle$, we start by assuming that the surface differential is constant and equal to Equation (81). Then [21]

$$\langle |I|^2 \rangle \approx \iint_F \iint_{F'} e^{j\left[q_x(x-x') + q_y(y-y')\right]} \langle e^{jq_z(z-z')} \rangle dS dS'. \tag{84}$$

Furthermore, we are working in a facet-local reference frame such that $\bar{z} = \bar{z}' = 0$. As a result, $z = \zeta$ and $z' = \zeta'$ are jointly distributed according to a two-dimensional autocorrelated Gaussian process with zero mean. This process is known to have a characteristic function equal to

$$\langle e^{jq_z(z-z')} \rangle = e^{-q_z^2 s^2 (1-\rho)}, \tag{85}$$

where s and ρ are defined as in Section II.A and denote the rms height and surface autocorrelation function. Substituting Equation (85) into Equation (84) yields

$$\langle |I|^2 \rangle = e^{-q_z^2 s^2} \iint_F \iint_{F'} e^{j\left[q_x(x-x') + q_y(y-y')\right] + q_z^2 s^2 \rho(x-x', y-y'))} dS dS'. \tag{86}$$

This result, first provided by Ulaby et al. in [4], p. 934, cannot be solved analytically for any of the autocorrelation functions provided in Section II.A, so further approximations are necessary to yield a closed-form solution. For instance, under the GO model, it is typically assumed that $q_z^2 s^2 \gg 1$ so that the contribution of $\rho(\xi)$ in the integrand can be neglected for large values of ξ. This follows from the fact that under the GO approximation, $\lambda \to 0$, so

$$q_z^2 s^2 = \frac{4\pi^2}{\lambda^2} (\cos\theta_i + \cos\theta_s)^2 s^2 \to \infty \tag{87}$$

---

[21] Note that in this derivation, we have implicitly assumed that the terrain surface and the terrain slopes are independent from each other. Refer to Appendix V for more details on this approximation.

for typical angles of incidence and reflection. Also, this allows Ulaby et al. to approximate $\rho(\xi)$ by the first two terms of its Taylor expansion, which results in a closed-form solution for $\langle |I|^2 \rangle$ when facets are shaped like squares.

Unfortunately, these simplifications are not valid in this article because (1) the proposed terrain model uses triangular facets instead of square facets and, more importantly, (2) we are particularly interested in the RCS of a facet at grazing angles. In other words, we are interested in a region of operation where θ_i and θ_s tend to 90°, which results in $q_z^2 s^2 \to 0$ for finite λ. Note that under the true GO approximation, where $\lambda \to \infty$, $q_z^2 s^2$ will asymptotically tend to (see Appendix III)

$$\lim_{\substack{\lambda \to 0 \\ \theta_i, \theta_s \to 90}} (q_z s)^2 = 16\pi^2 s^2 \tag{88}$$

which will always be $\gg 1$ except for very small values of the surface roughness. This correctly captures the intuition that under the GO, there is no coherent reflected component unless the reflecting surface is (almost) perfectly flat.

Given this discussion, we now provide a new derivation of the facet RCS under the stationary phase approximation for large but finite λ, i.e., a quasi-GO approximation. It is inspired by previous results from Ulaby et al. and de Roo in the PO model [4, 3]. To start, we assume that the terrain autocorrelation function ρ is Gaussian (see Equation (3)). In that case,

$$e^{q_z^2 s^2 \rho} = \sum_{n=0}^{\infty} \frac{\left(q_z^2 s^2 \rho\right)^n}{n!} = 1 + \sum_{n=1}^{\infty} \frac{(q_z s)^{2n}}{n!} \rho^n. \tag{89}$$

Substituting Equations (81) and (89) into Equation (86) and inverting the order of summation and integration yields

$$\langle |I|^2 \rangle = \left(1 + \left(\tfrac{2s}{l}\right)^2\right) e^{-(q_z s)^2} \left[I_0 + \sum_{n=1}^{\infty} \frac{(q_z s)^{2n}}{n!} I_n \right], \tag{90}$$

with

$$I_0 = \iint_F \iint_{F'} e^{j\left[q_x(x-x') + q_y(y-y')\right]} dA dA' \tag{91}$$

$$I_n = \iint_F \iint_{F'} \rho^n e^{j\left[q_x(x-x') + q_y(y-y')\right]} dA dA'. \tag{92}$$

Here, I_0 corresponds to the first term of the Taylor expansion of ρ ($n = 0$) and captures coherent scattering from all points in the facet. Indeed, by applying Equation (77), we see that

$$\langle \sigma \rangle \propto I_0 + \sum_{n=1}^{\infty} \frac{(q_z s)^{2n}}{n!} I_n. \tag{93}$$

Also, we can now directly map these terms to the coherent and non-coherent

scattering in Equation (7) to obtain

$$\langle |E_{s,i}| \rangle^2 \propto I_0 = \left| \iint_F e^{j(q_x x + q_y y)} dxdy \right|^2 \tag{94}$$

$$\mathrm{Var}\{E_{s,i}\} \propto \sum_{n=1}^{\infty} \frac{(q_z s)^{2n}}{n!} I_n. \tag{95}$$

Finally, observe that if the facet is perfectly flat, i.e., $s = 0$, then the non-coherent term vanishes. This result is consistent with real-life intuition because it is known that electrically large flat surfaces produce coherent reflections that are well modeled by the laws of oblique reflection.

8. Non-Coherent Term of the Phase Integral

To evaluate the non-coherent term of the phase integral, we follow the procedure outlined by Ulaby et al. in [4] and assume that ρ decays fast compared to the dimensions of the facet (i.e., $l \ll L$, where L is the smallest side of the facet). Under this approximation, the limits of integration in I_n can be replaced by a square facet of side $2L$ without incurring in large errors even if the actual facet is a triangle instead of a square. Therefore,

$$\begin{aligned} I_n &\approx \int_{-L}^{L}\int_{-L}^{L}\int_{-L}^{L}\int_{-L}^{L} e^{-n\frac{(x-x')^2+(y-y')^2}{l^2}+j\left[q_x(x-x')+q_y(y-y')\right]} dxdydx'dy' \\ &= \int_{-L}^{L}\int_{-L}^{L}\int_{-L-x'}^{L-x'}\int_{-L-y'}^{L-y'} e^{-n\frac{u^2+v^2}{l^2}+j[q_x u+q_y v]} dudvdx'dy'. \end{aligned} \tag{96}$$

Using Fubini's theorem, plus the fact that ([4], p. 934)

$$\int_{-L}^{L}\int_{-L-x'}^{L-x'} e^{jq_x u} f(u) du dx' = \int_{-2L}^{2L} (2L - |u|)\, f(u) e^{jq_x u} du, \tag{97}$$

we get

$$I_n \approx \int_{-2L}^{2L}\int_{-2L}^{2L} (2L - |u|)\,(2L - |v|)\, e^{-n\frac{u^2+v^2}{l^2}+j[q_x u+q_y v]} dudv. \tag{98}$$

But because $e^{-n\frac{u^2+v^2}{l^2}}$ decays to zero much faster than L, the integrand will only contribute to the integral for small values of $|u|$ and $|v|$, which allow us to approximate $(2L - |u|)\,(2L - |v|) \approx (2L)^2 = A_{\text{facet}}$. Similarly, the error introduced by letting L tend to infinity will also be small, so we conclude that

$$I_n \approx A_{\text{facet}} \int_{-\infty}^{\infty}\int_{-\infty}^{\infty} e^{-n\frac{u^2+v^2}{l^2}+j[q_x u+q_y v]} dudv. \tag{99}$$

This integral is simply the Fourier transform of a scaled Gaussian function, which can be shown to be equal to ([4], p. 938)

$$I_n \approx A_{\text{facet}} \frac{\pi l^2}{n} e^{-\frac{l^2}{4n}\left(q_x^2+q_y^2\right)}. \tag{100}$$

Next, we solve I_0 analytically with the restriction that the solution must be valid for any polygonal facet. To do so, we adapt the method proposed in [23], which leverages Green's theorem to perform integration over the facet contour rather than its area.

The proof is constructed as follows: First, we note that

$$\begin{aligned} I_0 &= \iint_F \iint_{F'} e^{j\left[q_x(x-x')+q_y(y-y')\right]} dA dA' = \\ &= \iint_F e^{j(q_x x+q_y y)} dx dy \iint_{F'} e^{-j\left(q_x x'+q_y y'\right)} dx' dy' \\ &= \left| \iint_F e^{j(q_x x+q_y y)} dx dy \right|^2 . \end{aligned} \tag{101}$$

Therefore, we can estimate I_0 by simply evaluating a phase integral over a polygonal facet F. To that end, let us recall Green's theorem for a simple region S:

$$\iint_S \left(\frac{\partial Q}{\partial x} - \frac{\partial P}{\partial y} \right) dA = \oint_C P dx + \oint_C Q dy, \tag{102}$$

where $P(x, y)$ and $Q(x, y)$ are two arbitrary functions over the region S, C denotes its contour, and the operator $\oint_C$ indicates that the line integral is computed over a positively oriented contour.

For the purposes of this article, let S be the polygonal facet of interest F (i.e., a triangle in the 3D mesh), let P and Q be defined as

$$\frac{\partial Q}{\partial x} = j q_x e^{j(q_x x+q_y y)} \tag{103}$$

$$\frac{\partial Q}{\partial y} = j q_y e^{j(q_x x+q_y y)}, \tag{104}$$

and let C be the facet's contour, expressed as a collection of straight sides such that the i-th side can be parametrically written as

$$x_i(t) = (1-t)x_i + t x_{i+1 \bmod \mathrm{N}} = x_i + \Delta x_i t \tag{105}$$

$$y_i(t) = (1-t)y_i + t y_{i+1 \bmod \mathrm{N}} = y_i + \Delta y_i t. \tag{106}$$

In this notation, $t \in [0, 1)$ is the parametric variable; N is equal to the number of sides in the polygon; (x_i, y_i), $i \in [1, N]$ represent the coordinates of the facet as given by the three-dimensional mesh described in Section II.A.1; and $\Delta x_i = x_{i+1 \bmod \mathrm{N}} - x_i$ and $\Delta y_i = y_{i+1 \bmod \mathrm{N}} - y_i$ represent the discrete differentials in the x and y direction, which are also dictated by the three-dimensional mesh.

Next, we apply Green's theorem to obtain:

$$\iint_F \left(j q_x e^{j(q_x x+q_y y)} - j q_y e^{j(q_x x+q_y y)} \right) = \oint_C e^{j(q_x x+q_y y)} dx + \oint_C e^{j(q_x x+q_y y)} dy, \tag{107}$$

which yields

$$\iint_F e^{j(q_x x+q_y y)} dx dy = \frac{1}{j\,(q_x - q_y)} \left[\oint_C e^{j(q_x x+q_y y)} dx + \oint_C e^{j(q_x x+q_y y)} dy \right]. \tag{108}$$

Furthermore, because we have assumed a polygonal facet, its contour is just the sum of N edges. As a result,

$$\begin{aligned}\oint_C e^{j(q_x x+q_y y)}dx &= \sum_{i=1}^{N}\int_0^1 e^{j(q_x x_i(t)+q_y y_i(t))}\frac{dx_i(t)}{dt}dt \\ &= \sum_{i=1}^{N}\Delta x_i e^{j(q_x x_i+q_y y_i)}\int_0^1 e^{j(q_x\Delta x_i t+q_y\Delta y_i t)}dt \\ &= \sum_{i=1}^{N}\Delta x_i e^{j(q_x x_i+q_y y_i)}e^{j\frac{\delta_i}{2}}\frac{\sin(\delta_i/2)}{\delta_i/2} \\ &= \sum_{i=1}^{N}\Delta x_i e^{j\alpha_i}\mathrm{sinc}(\beta_i),\end{aligned} \tag{109}$$

where $\mathrm{sinc}(\cdot)$ denotes to the unnormalized sinc function

$$\mathrm{sinc}(x) = \frac{\sin x}{x} \tag{110}$$

and

$$\delta_i = q_x\Delta x_i t + q_y\Delta y_i t \tag{111}$$

$$\alpha_i = q_x\frac{x_{i+1 \bmod \mathrm{N}}+x_i}{2} + q_y\frac{y_{i+1 \bmod \mathrm{N}}+y_i}{2} \tag{112}$$

$$\beta_i = q_x\frac{x_{i+1 \bmod \mathrm{N}}-x_i}{2} + q_y\frac{y_{i+1 \bmod \mathrm{N}}-y_i}{2}. \tag{113}$$

Note that α_i and β_i only depend on the vertices of a facet, for which we have well-defined coordinates thanks to the surface DEM. Therefore, they can be easily calculated and used to evaluate Equation (109). Also, the exact same procedure can be used to derive the fact that

$$\oint_C e^{j(q_x x+q_y y)}dy = \sum_{i=1}^{N}\Delta y_i e^{j\alpha_i}\mathrm{sinc}(\beta_i). \tag{114}$$

Consequently,

$$\iint_F e^{j(q_x x+q_y y)}dxdy = \frac{1}{j(q_x-q_y)}\sum_{i=1}^{N}(\Delta x_i+\Delta y_i)e^{j\alpha_i}\mathrm{sinc}(\beta_i), \tag{115}$$

which finally leads to [22]

$$I_0 = \frac{1}{|q_x-q_y|^2}\left|\sum_{i=1}^{N}(\Delta x_i+\Delta y_i)e^{j\alpha_i}\mathrm{sinc}(\beta_i)\right|^2. \tag{116}$$

10. Summary of Results

In this section, we have studied the RCS of a rough horizontally oriented facet under a quasi-GO model. Starting from the Stratton-Chu equation, we have shown that at

[22] In Appendix VI, we show that this result is consistent with previously derived equations for square facets.

high-frequencies, we can estimate the expected total facet RCS in a given polarization as the sum of a coherent and a non-coherent component:

$$\langle \sigma \rangle = \langle \sigma_{coh} \rangle + \langle \sigma_{ncoh} \rangle \tag{117}$$

with

$$\langle \sigma_{coh} \rangle = \left(1 + \tfrac{4s^2}{l^2}\right) \frac{k^2}{4\pi} \frac{e^{-(q_z s)^2}}{|q_x - q_y|^2} E \left| \sum_{i=1}^{N} (\Delta x_i + \Delta y_i)\, e^{j\alpha_i} \mathrm{sinc}\,(\beta_i) \right|^2 \tag{118}$$

$$\langle \sigma_{ncoh} \rangle = \left(1 + \tfrac{4s^2}{l^2}\right) \left(\frac{kl}{2}\right)^2 e^{-(q_z s)^2} A_{\text{facet}} E \sum_{n=1}^{\infty} \frac{(q_z s)^{2n}}{n! n} e^{-\frac{l^2}{4n}\left(q_x^2 + q_y^2\right)}, \tag{119}$$

and

$$E = \left[|p_{11} e_h + p_{12} e_v|^2 + |p_{21} e_h + p_{22} e_v|^2 \right]. \tag{120}$$

Note that this RCS, as currently stated, includes the effects of the polarizer in the receiving antenna. Therefore, it can be used directly in link budget calculations to estimate the received power from the lunar terrain.

B. RCS of an Arbitrarily Oriented Rough Facet

In the previous section, we derived the RCS of a rough facet assuming that it is oriented horizontally (i.e., $\hat{\boldsymbol{n}} = \hat{\boldsymbol{z}}$). We now extend this formulation so that facets can be tilted in arbitrary directions. These results are inspired by previous work from Ulaby et al. [24] and Kbenchaf [25].

1. Polarization Vectors

To start the discussion, let us first define the polarization vectors of the incident wave and scattered waves for an arbitrarily oriented facet using the FSA convention. However, unlike Section IV.A, let us now assume that we are calculating all these vectors in the antenna-local CRS, which is common to all facets in the terrain DEM.

A total of 12 vectors is required to estimate the RCS of an arbitrarily oriented facet. The first six define the polarization and direction of propagation of the incident and scattered EM wave. They are defined as follows:

- $\hat{\boldsymbol{k}}_i$ is the incidence unitary vector originating at the transmitter and pointing towards the barycenter of the facet.
- $\hat{\boldsymbol{h}}_i$ is the horizontal polarization vector of the incident wave, defined as $\hat{\boldsymbol{h}}_i = \frac{\hat{\boldsymbol{z}} \times \hat{\boldsymbol{k}}_i}{\left|\hat{\boldsymbol{z}} \times \hat{\boldsymbol{k}}_i\right|}$.
- $\hat{\boldsymbol{v}}_i$ is the vertical polarization vector of the incident wave, defined as $\hat{\boldsymbol{v}}_i = \hat{\boldsymbol{h}}_i \times \hat{\boldsymbol{k}}_i$.
- $\hat{\boldsymbol{k}}_s$ is the scattered unitary vector originating at the facet barycenter and pointing towards the receiver.

- $\hat{\boldsymbol{h}}_s$ is the horizontal polarization vector of the scattered wave, defined as $\hat{\boldsymbol{h}}_s = \frac{\hat{\boldsymbol{z}} \times \hat{\boldsymbol{k}}_s}{\left|\hat{\boldsymbol{z}} \times \hat{\boldsymbol{k}}_s\right|}$.
- $\hat{\boldsymbol{v}}_s$ is the vertical polarization vector of the incident wave, defined as $\hat{\boldsymbol{v}}_s = \hat{\boldsymbol{h}}_s \times \hat{\boldsymbol{k}}_s$.

Next, we define the polarization vectors with respect to a tilted facet. By definition of the FSA convention, the vertical polarization lies in the plane of incidence, while the parallel polarization is perpendicular to it [26]. Therefore,

- $\hat{\boldsymbol{a}}_i$ is the incidence unitary vector originating at the transmitter and pointing towards the barycenter of the facet. It is equal to $\hat{\boldsymbol{k}}_i$.
- $\hat{\boldsymbol{b}}_i$ is the horizontal polarization vector of the incident wave, defined as $\hat{\boldsymbol{h}}_i = \frac{\hat{\boldsymbol{n}} \times \hat{\boldsymbol{a}}_i}{|\hat{\boldsymbol{n}} \times \hat{\boldsymbol{a}}_i|}$.
- $\hat{\boldsymbol{c}}_i$ is the vertical polarization vector of the incident wave, defined as $\hat{\boldsymbol{c}}_i = \hat{\boldsymbol{b}}_i \times \hat{\boldsymbol{a}}_i$.
- $\hat{\boldsymbol{a}}_s$ is the scattered unitary vector originating at the facet barycenter and pointing towards the receiver. It is equal to $\hat{\boldsymbol{k}}_s$.
- $\hat{\boldsymbol{b}}_s$ is the horizontal polarization vector of the scattered wave, defined as $\hat{\boldsymbol{b}}_s = \frac{\hat{\boldsymbol{n}} \times \hat{\boldsymbol{k}}_s}{\left|\hat{\boldsymbol{n}} \times \hat{\boldsymbol{k}}_s\right|}$.
- $\hat{\boldsymbol{c}}_s$ is the vertical polarization vector of the incident wave, defined as $\hat{\boldsymbol{c}}_s = \hat{\boldsymbol{b}}_s \times \hat{\boldsymbol{a}}_s$.

Note that the only difference between the basis $(\hat{\boldsymbol{k}}_i, \hat{\boldsymbol{h}}_i, \hat{\boldsymbol{v}}_i)$ and the basis $(\hat{\boldsymbol{a}}_i, \hat{\boldsymbol{b}}_i, \hat{\boldsymbol{c}}_i)$ is that the former is computed using the vector $\hat{\boldsymbol{z}}$, while the latter is calculated with the facet normal $\hat{\boldsymbol{n}}$, which is not equal to $\hat{\boldsymbol{z}}$ because the facet is tilted (the same is also true for the bases of the scattered wave). This differentiation is necessary because the perpendicular and parallel Fresnel reflection coefficients, as defined by the theory of oblique incidence, refer to the polarization vectors $\hat{\boldsymbol{b}}_i$ and $\hat{\boldsymbol{c}}_i$ instead of $\hat{\boldsymbol{h}}_i$ and $\hat{\boldsymbol{v}}_i$.

Finally, 12 additional vectors can be calculated for each individual facet in the DEM, representing the polarization vectors in a facet-local CRS. For ease of notation, these are denoted with an apostrophe (i.e., $\hat{\boldsymbol{k}}_i$ vs. $\hat{\boldsymbol{k}}_i'$) and can be calculated by applying the rotation matrix (one per facet) that transforms from the antenna-local CRS to the facet-local CRS.

2. Incident Electric Field

To calculate the scattered field, we start by defining the incident wave on a single facet. Just as in Section IV.A, we assume this wave to be planar so that

$$\mathbf{E}_i = E_0 e^{-jk\hat{\boldsymbol{k}}_i \cdot \boldsymbol{r}} \left(\alpha_h \hat{\boldsymbol{h}}_i + \alpha_v \hat{\boldsymbol{v}}_i \right), \tag{121}$$

with E_0, α_h, and α_v defined as in Section IV.A.1. This incident wave needs to be decomposed into the vertical and polarization vectors of the tilted facet. This results in

$$\begin{aligned}\mathbf{E}_i =& E_0 e^{-jk\hat{\boldsymbol{k}}_i\cdot\boldsymbol{r}}\left[\left(\alpha_h\hat{\boldsymbol{h}}_i\cdot\hat{\boldsymbol{b}}_i+\alpha_v\hat{\boldsymbol{v}}_i\cdot\hat{\boldsymbol{b}}_i\right)\hat{\boldsymbol{b}}_i+\left(\alpha_h\hat{\boldsymbol{h}}_i\cdot\hat{\boldsymbol{c}}_i+\alpha_v\hat{\boldsymbol{v}}_i\cdot\hat{\boldsymbol{c}}_i\right)\hat{\boldsymbol{c}}_i\right]\\ =& E_0 e^{-jk\hat{\boldsymbol{k}}_i\cdot\boldsymbol{r}}\left(\epsilon_b\hat{\boldsymbol{b}}_i+\epsilon_c\hat{\boldsymbol{c}}_i\right).\end{aligned} \tag{122}$$

3. Scattered Electric Field

Let $\boldsymbol{R}$ define the rotation matrix that transforms from the antenna-centered CRS to the facet-local CRS.[23] Then the incident electric field in the facet-local CRS can be estimated as

$$\mathbf{E}_i' = \boldsymbol{R}\mathbf{E}_i = E_0 e^{-jk\hat{\boldsymbol{k}}_i'\cdot\boldsymbol{r}'}\left(\epsilon_b\hat{\boldsymbol{b}}_i'+\epsilon_c\hat{\boldsymbol{c}}_i'\right). \tag{123}$$

Furthermore, in this facet-local CRS the facet is, by construction, placed in the xy plane. Therefore, all the results from Section IV.A are applicable, and the scattered electric field under the GO and KA approximation becomes

$$\mathbf{E}_s' = KE_0 I'\boldsymbol{p}' \tag{124}$$

where K is defined as in Equation (63) and

$$\boldsymbol{p}' = \left[\left(\alpha_h U_{hh}+\alpha_v U_{hv}\right)\hat{\boldsymbol{b}}_s'+\left(\alpha_h U_{hv}+\alpha_v U_{vv}\right)\hat{\boldsymbol{c}}_s'\right]. \tag{125}$$

Note that the factors U_{hh}, U_{hv}, U_{vh}, and U_{vv} depend only on the dot product between two vectors. Therefore, because the dot product is an invariant operation with respect to rotation, the value of these constants can be computed in the facet-local or antenna-centered CRS. On the other hand, I' denotes the phase integral, which depends on the individual components of vector $\boldsymbol{q}'$, as defined in Equation (54). Consequently, in general, I calculated in the antenna-centered CRS will be different from I' calculated in the facet-local CRS, and the latter must be used to estimate the scattered field by an arbitrarily oriented facet.

Next, we rotate the polarization vector $\boldsymbol{p}'$ back to the antenna-local CRS

$$\mathbf{E}_s = KE_0 I'\boldsymbol{R}^T\boldsymbol{p}' = KE_0 I'\left[\left(\alpha_h U_{hh}+\alpha_v U_{hv}\right)\hat{\boldsymbol{b}}_s+\left(\alpha_h U_{hv}+\alpha_v U_{vv}\right)\hat{\boldsymbol{c}}_s\right], \tag{126}$$

and express the wave's polarization in terms of $\hat{\boldsymbol{h}}_s$ and $\hat{\boldsymbol{v}}_s$ instead of $\hat{\boldsymbol{b}}_s$ and $\hat{\boldsymbol{c}}_s$. This yields

$$\begin{aligned}\mathbf{E}_s =& KE_0 I'\left[\left(\alpha_h U_{hh}+\alpha_v U_{hv}\right)\hat{\boldsymbol{b}}_s\cdot\hat{\boldsymbol{h}}_s+\left(\alpha_h U_{hv}+\alpha_v U_{vv}\right)\hat{\boldsymbol{c}}_s\cdot\hat{\boldsymbol{h}}_s\right]\hat{\boldsymbol{h}}_s\\ &+KE_0 I'\left[\left(\alpha_h U_{hh}+\alpha_v U_{hv}\right)\hat{\boldsymbol{b}}_s\cdot\hat{\boldsymbol{v}}_s+\left(\alpha_h U_{hv}+\alpha_v U_{vv}\right)\hat{\boldsymbol{c}}_s\cdot\hat{\boldsymbol{v}}_s\right]\hat{\boldsymbol{v}}_s\\ =& KE_0 I'\left[\gamma_h\hat{\boldsymbol{h}}_s+\gamma_v\hat{\boldsymbol{v}}_s\right].\end{aligned} \tag{127}$$

Note that this result is equivalent to what was obtained in Section IV.A with the exception that the multiplicative constants for $\hat{\boldsymbol{h}}_s$ and $\hat{\boldsymbol{v}}_s$ are corrected due to the facet tilt (refer to Equation (66)).

---

[23] As previously stated, there is one such matrix per facet in the terrain mesh. However, we attach no facet-related index to any of the variables of this section to ease notation.

4. Received Electric Field

The derivation of the received electric field in the case of a rough tilted surface is analogous to what is presented in Section IV.A.4, with the exception that I is replaced by I' and $\boldsymbol{\zeta}$ is replaced by

$$\boldsymbol{\Gamma} = \begin{bmatrix} \gamma_h \\ \gamma_v \end{bmatrix} = \begin{bmatrix} (\alpha_h U_{hh} + \alpha_v U_{hv})\, \hat{\boldsymbol{b}}_s \cdot \hat{\boldsymbol{h}}_s + (\alpha_h U_{hv} + \alpha_v U_{vv})\, \hat{\boldsymbol{c}}_s \cdot \hat{\boldsymbol{h}}_s \\ (\alpha_h U_{hh} + \alpha_v U_{hv})\, \hat{\boldsymbol{b}}_s \cdot \hat{\boldsymbol{v}}_s + (\alpha_h U_{hv} + \alpha_v U_{vv})\, \hat{\boldsymbol{c}}_s \cdot \hat{\boldsymbol{v}}_s \end{bmatrix}. \tag{128}$$

Therefore, and assuming that the receiver's antenna perfectly rejects the cross-polarization, we obtain a received electric field:

$$\mathbf{E}_r = K E_0 I' \sqrt{G_{co}} \left[(p_{11}^{co} \gamma_h + p_{12}^{co} \gamma_v)\, \hat{\boldsymbol{h}}_s + (p_{21}^{co} \gamma_h + p_{22}^{co} \gamma_v)\, \hat{\boldsymbol{v}}_s \right], \tag{129}$$

where p_{ij}^{co} are the polarizer coefficients of the receiver's antenna.

5. Facet RCS

Finally, the expected facet RCS for an arbitrarily oriented rough facet can be estimated as

$$\langle \sigma \rangle = \langle \sigma_{coh} \rangle + \langle \sigma_{ncoh} \rangle \tag{130}$$

with

$$\langle \sigma_{coh} \rangle = \left(1 + \tfrac{4s^2}{l^2}\right) \frac{k^2}{4\pi} \frac{e^{-(q'_z s)^2}}{\left|q'_x - q'_y\right|^2} \Gamma \left| \sum_{i=1}^{N} (\Delta x'_i + \Delta y'_i)\, e^{j\alpha'_i} \mathrm{sinc}\,(\beta'_i) \right|^2 \tag{131}$$

$$\langle \sigma_{ncoh} \rangle = \left(1 + \tfrac{4s^2}{l^2}\right) \left(\frac{kl}{2}\right)^2 e^{-(q'_z s)^2} A_{\text{facet}} \Gamma \sum_{n=1}^{\infty} \frac{(q'_z s)^{2n}}{n! n} e^{-\frac{l^2}{4n}\left(q_x'^2 + q_y'^2\right)}, \tag{132}$$

and

$$\Gamma = \left[\left| p_{11}\gamma_h + p_{12}\gamma_v \right|^2 + \left| p_{21}\gamma_h + p_{22}\gamma_v \right|^2 \right]. \tag{133}$$

As before, the apostrophe operator indicates that the quantities to be substituted in these equations are expressed in the facet-local CRS, rather than the antenna-centered CRS.

V. Results

The model presented in Sections III and IV has been implemented in MATLAB© and used to simulate reflections from the lunar South Pole from a landed spacecraft. Table 1 summarizes the main inputs to the tool, including the transmit and receive antennas, the landing site, the carrier frequency, lunar soil dielectric constant, and the lunar terrain roughness properties. Note that a total of 92 simulations were carried out, one per day, in order to properly capture the relative motion of Earth in the sky as seen from the lunar surface.

Table 1. Simulation Parameters

Parameter	Value	Units	Comments
Carrier frequency	2.2	GHz	S-band
Landing site	Mount Malapert	-	-
Transmit antenna	Dipole	-	Half-wave
Transmit antenna height	10	m	Above surface
Transmit polarization	RCP	-	-
Receive antenna	DSN 34m	-	-
Receive polarization	RCP	-	-
Simulation start	1/1/2020	-	-
Simulation end	4/1/2020	-	-
Lunar terrain DEM resolution	10	m	-
Lunar terrain extent	6×6	km^2	-
Lunar dielectric constant	$3.7 - j0.01$	F/m	-
Lunar roughness	0.25	m	-
Lunar roughness distance	1	m	-

A. Reflected Power

Figure 9 plots the Earth elevation subtended by Earth over a three-month period and as seen from an antenna placed 10 m above the surface.[24] Observe that Earth almost never rises above 12° above the horizon approximately and even sets completely for about one week a month. Note that this plot has been obtained assuming that the receiver is placed at the center of Earth. In reality, however, there is a second-order variation in receiver elevation caused by the latitude at which the ground station is located, but the differences are small enough that they can be neglected for this analysis.

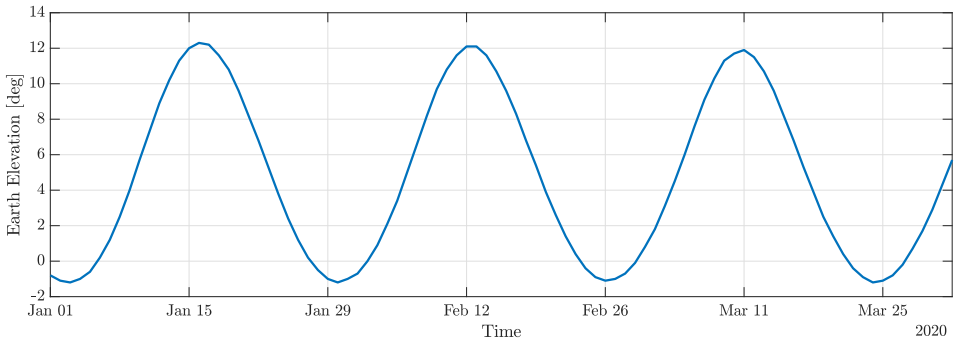

Figure 9. Earth Elevation at Mount Malapert

[24]The elevation angle calculation takes into account DEM, as well as the Moon curvature.

To study the amount of power reflected from the lunar surface, three metrics are defined from the notation of Section III:

$$\beta = \frac{\text{Total LoS power}}{\text{Total reflected power}} \qquad \propto \frac{|E_{los}|^2}{\langle |E_s|^2 \rangle} \tag{134}$$

$$\gamma = \frac{\text{Coherently reflected power}}{\text{Total reflected power}} \qquad \propto \frac{\langle \left|E_s^{coh}\right|^2 \rangle}{\langle |E_s|^2 \rangle} \tag{135}$$

$$K = \frac{\text{Coherent power}}{\text{Non-coherently reflected power}} \propto \frac{\langle \left|E_{los} + E_s^{coh}\right|^2 \rangle}{\langle |E_s^{ncoh}|^2 \rangle}. \tag{136}$$

β is a "lump-sum" metric that simply indicates the ratio between the amount of power from the LoS ray, compared to the amount of power received from reflections. γ, on the other hand, is a number from 0 to 100% that indicates the amount of reflected power that has been coherently reflected from the surface. Finally, K is equal to the Rice Factor as defined in Equation (33) and can be used to estimate statistics of the received signal. Note that, in these equations, the power of the LoS ray has been adjusted to account for diffraction loss effects following the discussion from Section III.D.

Figure 10 shows the simulation results for the three aforementioned metrics. All timelines are synchronized with the motion of Earth in the lunar sky. Several conclusions are possible:

- The amount of reflected power is clearly driven by the Earth elevation angle. In general, three regions can be identified:
  - At high elevation angles, reflections from the lunar surface dominate. They are strong enough to result in $\beta \approx 5$ dB.
  - When the Earth elevation angle is $< 1°$, the diffraction effects dominate. They reduce the power of the LoS ray and cause β to tend to 0.
  - When Earth is located at $\sim 1°$ of elevation, β increases significantly. This is due to the fact that the reflection angles from facets located between the lunar lander and Earth are oriented in such a way that almost no reflections occur (e.g., they are downward sloping). Note that this is probably an artifact created by the input DEM, which we assumed to be error free, and highlights the model sensitivity of the terrain when reflections are estimated at near-grazing angles. Additional modeling efforts would be required to eliminate these artifacts, either by taking into account uncertainty in the DEM analytically in a statistical fashion, or by conducting Monte Carlo experiments over uncertain terrain realizations and then averaging them.
- When the elevation angle decreases below $\sim 5°$, the multipath fading process is dominated by coherent reflections (i.e., γ tends to 1). This can also be observed using the Rice Factor, which quickly grows to over 50 dB.

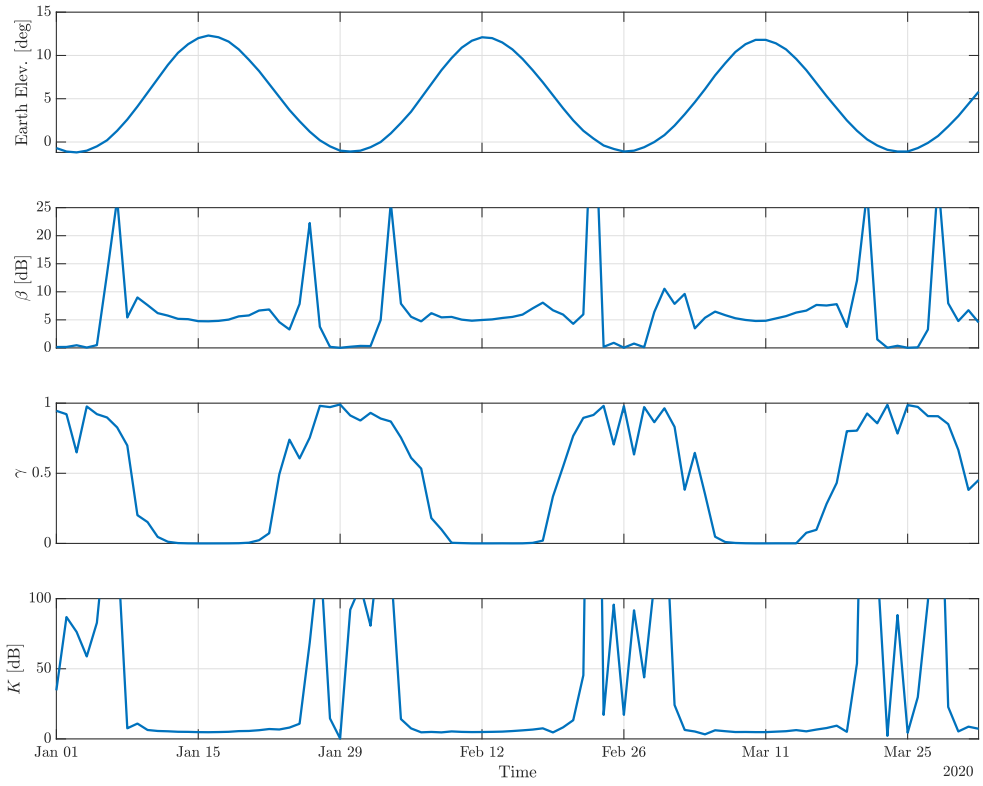

Figure 10. Reflected Power over Time

- At high elevation angles, incoherent reflections dominate. Therefore, the channel is well modeled by a Rician random variable with a Rice Factor of approximately $K \approx 5$ dB.

Observe that these results cannot be generalized. Indeed, changing the carrier frequency, the radiation pattern of the transmit antenna, or even the landing site, will significantly alter the estimates for total reflected and diffracted power. Therefore, the results presented here should be viewed as a best-guess estimate from an engineering model and should not, in any case, be interpreted as "the truth."

Finally, all results obtained from the proposed model seem to agree with engineering intuition except for the increase in β when the Earth elevation is around 1°. To understand why this happens, we note that at this elevation angle, neither reflection nor diffraction dominate. Indeed, the elevation angle is so low that only a handful of facets right in front of the landed spacecraft will satisfy the conditions of specular reflection, so the total reflected power decreases and the channel conditions improve.

B. Channel Delay and Doppler Spread

The results of the simulation engine can also be used to estimate the channel Doppler and delay profile, and their respective summary metrics, the average delay and Doppler, and the delay and Doppler spread. These last metrics are interesting from a communications standpoint because they are inversely related to the channel coherence bandwidth and channel coherence time, respectively [13].

In general, the average delay and Doppler are defined as follows [13]:

$$\bar{\tau} = \frac{1}{P} \int_{-\infty}^{\infty} \tau p(\tau) d\tau \tag{137}$$

$$\bar{f} = \frac{1}{P} \int_{-\infty}^{\infty} f p(f) df, \tag{138}$$

where τ and f denote the relative delay and Doppler shift with respect to the LoS ray, P denotes the total reflected power, and $p(\tau)$ and $p(f)$ denote the received power spectral density of the reflections as a function of propagatoin delay and Doppler shift. Similarly, the delay and Doppler spread are defined as

$$\sigma_\tau^2 = \frac{1}{P} \int_{-\infty}^{\infty} \left(\tau - \bar{\tau}\right)^2 p(\tau) d\tau \tag{139}$$

$$\sigma_f^2 = \frac{1}{P} \int_{-\infty}^{\infty} \left(f - \bar{f}\right)^2 p(f) df \tag{140}$$

Because our simulation engine calculates reflection effects via a collection of N rays, these equations can be approximated in the discrete domain as:

$$\bar{\tau} \approx \frac{1}{P} \sum_{i=0}^{N} \tau_i P_i \tag{141}$$

$$\bar{f} \approx \frac{1}{P} \sum_{i=0}^{N} f_i P_i, \tag{142}$$

where τ_i, f_i, and P_i denote the relative delay, relative Doppler shift, and power of the i-th reflected ray. Similarly,

$$\sigma_\tau^2 \approx \frac{1}{P} \sum_{i=0}^{N} (\tau_i - \bar{\tau}) P_i \tag{143}$$

$$\sigma_f^2 \approx \frac{1}{P} \sum_{i=0}^{N} (f_i - \bar{f}) P_i \tag{144}$$

Note that these equations are approximations not just because they are obtained from a finite collection of rays. Indeed, because of limitations in the estimation of P_i, they also fail to properly account for diffraction effects at very low elevation angles and are

subject to the limitations inherent to the approximations made while deriving a facet RCS.

Figure 11 plots the result of these calculations for the scenario from Table 1. Observe that the typical delay spread is less than 1 μs, while the Doppler spread is estimated at less than 0.01 Hz. Note also that this small Doppler spread is caused here because the spacecraft on the lunar surface is assumed to be stationary, i.e., higher Doppler spreads would be experienced in the case of a rover that moves around the lunar surface depending on the maximum roving speed. Finally, note that the provided plots have gaps at regularly spaced time intervals. These correspond to periods of time when Earth is below the horizon, so the calculation of the Doppler and delay spread is considered invalid.

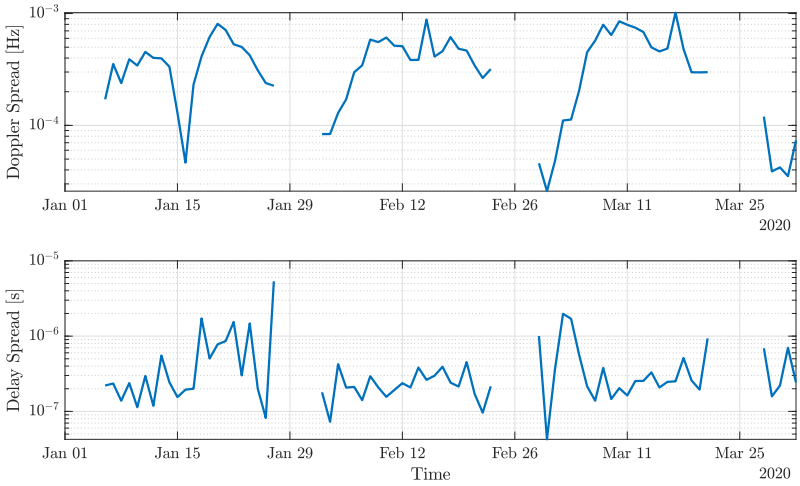

Figure 11. Delay and Doppler Spread

VI. Conclusions

This paper presents a new simulation model to estimate the characteristics of a multipath fading channel from a spacecraft on the surface of a planetary body such as the Moon. The model takes as input a DEM of the surface, along with its dielectric and roughness properties, and provides a full channel characterization that includes the total reflected power, the fraction of power coherently and incoherently reflected, and the Doppler and delay shifts experienced by the reflections.

Internally, the proposed simulation model is built around the theory of scattering from rough and random dielectric surfaces. It utilizes a quasi-GO approximation of the reflected far fields to estimate the total power reflected along with the Doppler and delay characteristics. It also includes a simplified knife-edge diffraction model to estimate the power loss due to diffraction at very low elevation angles.

While the results presented in Section V are consistent with engineering intuition, a

complete experimental validation of the model is still pending and will require comparison with data collected from landed spacecraft like VIPER, or orbiting spacecraft like the Lunar Reconnaissance Orbiter (LRO) or the EM-1 Cubesats. Therefore, the results presented in this article must, for now, be considered an engineering effort to provide credible multipath fading models for mission design and analysis while measurements from actual flight operations are not available.

Acknowledgments

I would like to thank Rob Manning and Curtis Chen, from the Jet Propulsion Laboratory, for pointing me in the right direction for this research, including past literature in the field of radar, radio science, and remote sensing. I would also like to thank Curtis Chen for his invaluable comments during the review process.

The research was carried out at the Jet Propulsion Laboratory, California Institute of Technology, under a contract with the National Aeronautics and Space Administration (80NM0018D0004).

References

[1] Massachusetts Institute of Technology, "LOLA PDS Archive," http://imbrium.mit.edu/, 2021.

[2] F. Ulaby and D. Long, *Microwave radar and radiometric remote sensing*. Artech House, 2015.

[3] R. D. de Roo, "Theory and measurement of bistatic scattering of x-band microwaves from rough dielectric surfaces," Ph.D. dissertation, University of Michigan, 1996.

[4] F. T. Ulaby, R. K. Moore, and A. K. Fung, *Microwave remote sensing active and passive-volume II: radar remote sensing and surface scattering and enission theory*. Artech House, Inc., 1982.

[5] A. Y. Nashashibi and F. T. Ulaby, "MMW polarimetric radar bistatic scattering from a random surface," *IEEE transactions on geoscience and remote sensing*, vol. 45, no. 6, pp. 1743–1755, 2007.

[6] D.-T. Lee and B. J. Schachter, "Two algorithms for constructing a delaunay triangulation," *International Journal of Computer & Information Sciences*, vol. 9, no. 3, pp. 219–242, 1980.

[7] M. P. Clarizia, C. Gommenginger, M. Di Bisceglie, C. Galdi, and M. A. Srokosz, "Simulation of l-band bistatic returns from the ocean surface: A facet approach with application to ocean gnss reflectometry," *IEEE Transactions on Geoscience and Remote Sensing*, vol. 50, no. 3, pp. 960–971, 2011.

[8] T. Möller and B. Trumbore, "Fast, minimum storage ray-triangle intersection," *Journal of graphics tools*, vol. 2, no. 1, pp. 21–28, 1997.

[9] "pyproj," https://pyproj4.github.io/pyproj/stable/, 2021.

[10] "spice," https://naif.jpl.nasa.gov/naif/toolkit.html, 2021.

[11] G. L. Stuber, *Principles of Mobile Communication*. Kluwer Academic Publishers, 2001.

[12] Goddard Space Flight Center, "The Doppler Equation in Range and Range Rate Measurements," NASA, Tech. Rep. X-507-65-385, October 1965. https://ntrs.nasa.gov/archive/nasa/casi.ntrs.nasa.gov/19660010159.pdf

[13] T. S. Rappaport, *Wireless Communications: Principles & Practice*. Prentice Hall PTR, 1996.

[14] Y. Z. Umul, "Comparison of diffraction methods for lunar occultations," *Optik*, vol. 205, p. 163756, 2020.

[15] L. E. Vogler, "Point-to-point communication on the moon," *J. Res. Bur. Stand., Sect. D*, vol. 67, pp. 5–21, 1963.

[16] J. F. Lindsey, "Lunar surface transmission loss for the apollo astronaut," Tech. Rep., 1968.

[17] H. T. Dougherty and L. J. Maloney, "Application of diffractions by convex surfaces to irregular terrain situations," *Radio Science Journal of Research*, 1964.

[18] S. Rice, "Diffraction of plane radio waves by a parabolic cylinder: Calculation of shadows behind hills," *Bell System Technical Journal*, vol. 33, no. 2, pp. 417–504, 1954.

[19] J. B. Keller, "Geometrical theory of diffraction," *Josa*, vol. 52, no. 2, pp. 116–130, 1962.

[20] P. H. Pathak, G. Carluccio, and M. Albani, "The uniform geometrical theory of diffraction and some of its applications," *IEEE Antennas and Propagation magazine*, vol. 55, no. 4, pp. 41–69, 2013.

[21] J. Crysdale, "Comparison of some experimental terrain diffraction losses with predictions based on rice's theory for diffraction by a parabolic cylinder," *IRE Transactions on Antennas and Propagation*, vol. 6, no. 3, pp. 293–295, 1958.

[22] M. Soja, "Electromagnetic models of bistatic radar scattering from rough surfaces with gaussian correlation function," 2009.

[23] W. Gordon, "Far-field approximations to the kirchoff-helmholtz representations of scattered fields," *IEEE Transactions on Antennas and Propagation*, vol. 23, no. 4, pp. 590–592, 1975.

[24] F. T. Ulaby, F. Kouyate, A. K. Fung, and A. J. Sieber, "A backscatter model for a randomly perturbed periodic surface," *IEEE Transactions on Geoscience and Remote Sensing*, no. 4, pp. 518–528, 1982.

[25] A. Kbenchaf, "Sea surface scattering for near-grazing incidence," in *Oceans' 99. MTS/IEEE. Riding the Crest into the 21st Century. Conference and Exhibition. Conference Proceedings (IEEE Cat. No. 99CH37008)*, vol. 3, IEEE, 1999, pp. 1452–1456.

[26] D. Bell and L. Tadjpour, "Multipath Mitigation on In Situ Communication Links," *The Interplanetary Network Progress Report*, vol. 42-151, Jet Propulsion Laboratory, Pasadena, CA, pp. 1–21, November 2002. https://ipnpr.jpl.nasa.gov/progress_report/42-151/151F.pdf

[27] P. U. Papoulis, Athanasios, *Probability, Rnadom Variables, and Stochastic Processes*. McGraw-Hill, 2002.

[28] C. W. Chen, "Approach for modeling coherent radar ground echoes in planetary landing simulations," *Journal of Spacecraft and Rockets*, vol. 55, no. 1, pp. 85–94, 2018.

APPENDICES

I. Far-Field Approximation

The exact solution for the radiated electromagnetic field given a set of current sources is a function of the well-known Green's dyadic function [4, 22]:

$$\chi = \frac{\exp\left(-jk\left|\boldsymbol{r}-\boldsymbol{r'}\right|\right)}{4\pi\left|\boldsymbol{r}-\boldsymbol{r'}\right|}, \tag{145}$$

where $\boldsymbol{r}$ and $\boldsymbol{r'}$ denote the position of the receiver and the origin, respectively. The distance between transmitter and receiver can be expanded to

$$\left|\boldsymbol{r}-\boldsymbol{r'}\right|^2 = r^2 + r'^2 - 2\boldsymbol{r}\cdot\boldsymbol{r'} = r^2\left[1+\tfrac{r'^2}{r^2} - 2\tfrac{\boldsymbol{r}\cdot\boldsymbol{r'}}{r^2}\right], \tag{146}$$

with $r = |\boldsymbol{r}|$ and $r' = |\boldsymbol{r'}|$. In the far field, $r' \ll r$ and therefore

$$|\boldsymbol{r}-\boldsymbol{r'}| \approx r\sqrt{1-\tfrac{\boldsymbol{r}\cdot\boldsymbol{r'}}{r^2}} \approx r - \boldsymbol{r}\cdot\boldsymbol{r'}. \tag{147}$$

The later equality follows from the fact that

$$\sqrt{1-x} = 1 - \frac{x}{2} - \frac{x^2}{8} - \frac{x^3}{16} - \frac{5x^4}{128} + ... \approx 1 - \frac{x}{2} \tag{148}$$

for small x. Therefore, we conclude that in the far-field

$$\chi \approx \frac{\exp\left(-jkr + jk\boldsymbol{r}\cdot\boldsymbol{r'}\right)}{4\pi r} = \frac{e^{-jkr}}{4\pi r}e^{jk\boldsymbol{r}\cdot\boldsymbol{r'}}, \tag{149}$$

which is the term utilized in the original Stratton-Chu integral.

II. Dielectric Properties of Propagation Media

This appendix provides a succinct summary of the EM parameters that characterize a material, as well as typical quantities useful in EM theory that are defined from them. It is provided here as ancillary information, following the discussion from reference [2].

Given any material, we introduce four characteristic parameters:

1. ε denotes the electrical permittivity, in farads per meter (F/m).
2. μ denotes the magnetic permeability in henry per meter (H/m).
3. ρ_v denotes the volume charge density in coulomb per cubic meter (C/m^3).
4. σ denotes the conductivity in siemens per meter (S/m).

In general, the complex permittivity of a material is expressed as

$$\varepsilon = \varepsilon' - j\left(\varepsilon'' + \frac{\sigma}{\omega}\right), \tag{150}$$

where $\omega = 2\pi f$ is the angular frequency. Similarly, the complex magnetic permeability is expressed as

$$\mu = \mu' - j\mu''. \tag{151}$$

It is convenient to express the electric permittivity and permeability of a material normalized to that of free space (vacuum), resulting in what is known as the relative permittivity and relative permeability:

$$\tilde{\varepsilon} = \frac{\varepsilon}{\varepsilon_0} = \frac{\varepsilon'}{\varepsilon_0} - j\left(\frac{\varepsilon''}{\varepsilon_0} + \frac{\sigma}{\omega\varepsilon_0}\right) = \tilde{\varepsilon}' - j\left(\tilde{\varepsilon}'' + \frac{\tilde{\sigma}}{\omega}\right) \tag{152}$$

$$\tilde{\mu} = \frac{\mu}{\mu_0} = \frac{\mu'}{\mu_0} - j\frac{\mu''}{\mu_0} = \tilde{\mu}' - j\tilde{\mu}'', \tag{153}$$

where $\varepsilon_0 \approx 8.854 \cdot 10^{-12}$ F/m and $\mu_0 \approx 1.257 \cdot 10^{-6}$ H/m denote the permittivity and permeability of free space. Note that, in this appendix, the tilde symbol is used to indicate that a value is relative.

These dielectric properties, together with Maxwell's equations, form the basis for what is known as the homogeneous wave equation, which states that for materials with no charge density (i.e., $\rho_v = 0$), EM waves propagate according to the following differential equations:

$$\nabla^2 \boldsymbol{E} - \gamma^2 \boldsymbol{E} = 0 \tag{154}$$

$$\nabla^2 \boldsymbol{H} - \gamma^2 \boldsymbol{H} = 0, \tag{155}$$

where $\boldsymbol{E}$ and $\boldsymbol{H}$ are the vectorial representations of the electric and magnetic fields, expressed in phasor notation. Furthermore, the propagation constant is defined as

$$\gamma^2 = -\omega^2 \mu\varepsilon. \tag{156}$$

While solving these differential equations, it is common to use several other quantities. Namely,

- the wavenumber is defined as $k^2 = -\gamma^2$ so that $k = \omega\sqrt{\mu\varepsilon}$;
- the intrinsic impedance is defined as $\eta = \frac{\omega\mu}{k} = \sqrt{\frac{\mu}{\varepsilon}}$ in ohms (Ω);
- the phase velocity is defined as $v_p = \frac{\omega}{k} = \frac{1}{\sqrt{\mu\varepsilon}}$;
- and the index of refraction is defined as $n = \frac{c}{v_p} = c\sqrt{\mu\varepsilon}$, where c denotes the speed of light.

In the vacuum, $\varepsilon = \varepsilon_0$, $\mu = \mu_0$, and the phase velocity is by definition equal to the speed of light c. Therefore,

$$c = \frac{1}{\sqrt{\varepsilon_0 \mu_0}} \approx 3 \cdot 10^8 \text{ m/s}. \tag{157}$$

Using this fact, together with the definition of the relative permittivity and the relative permeability, and the fact that $\omega = 2\pi f = \frac{2\pi c}{\lambda}$, we can rewrite the different quantities previously introduced as:

$$k = k_0\sqrt{\tilde{\mu}\tilde{\varepsilon}} \tag{158}$$

$$\eta = \eta_0\sqrt{\frac{\tilde{\mu}}{\tilde{\varepsilon}}} \tag{159}$$

$$v_p = \frac{c}{\sqrt{\tilde{\mu}\tilde{\varepsilon}}} \tag{160}$$

$$n = n_0\sqrt{\tilde{\mu}\tilde{\varepsilon}}, \tag{161}$$

where $\eta_0 = \sqrt{\frac{\mu_0}{\varepsilon_0}} = 377 \approx 120\pi\ \Omega$, $k_0 = \frac{2\pi}{\lambda}$, and $n_0 = 1$ denote the intrinsic impedance, wavenumber, and index of refraction of free space, respectively. Further simplifications are possible depending on the material or medium where the wave propagates. For instance, a pure dielectric and non-ferromagnetic material,[25] also known as lossless material, will exhibit $\tilde{\mu} = 1$ and $\tilde{\varepsilon}'' = \tilde{\sigma} = 0$. In contrast, a lossy medium is defined as having $\Im\{\varepsilon\} \neq 0$, which occurs, for instance, in conducting materials (i.e., $\sigma \neq 0$).

To study the properties of lossy materials, the propagation constant is generally decomposed into α, the medium's attenuation constant, and β, its phase constant:

$$\gamma = \alpha + j\beta \tag{162}$$

with

$$\alpha = \frac{2\pi}{\lambda}\sqrt{\frac{\tilde{\varepsilon}'}{2}\left(-1 + \sqrt{1+\zeta^2}\right)} \tag{163}$$

$$\beta = \frac{2\pi}{\lambda}\sqrt{\frac{\tilde{\varepsilon}'}{2}\left(+1 + \sqrt{1+\zeta^2}\right)} \tag{164}$$

and

$$\zeta = \frac{\tilde{\varepsilon}'' + \frac{\tilde{\sigma}}{\omega}}{\tilde{\varepsilon}'} = \frac{\varepsilon'' + \frac{\sigma}{\omega}}{\varepsilon'} \tag{165}$$

Some authors call ζ the loss tangent and express it as "$\tan\delta$" instead, where δ is the angle between the imaginary and real part of the dielectric constant.[26] Also, we can now use ζ to express all characteristic material properties as follows:

$$k = k_0\sqrt{\tilde{\varepsilon}'}\sqrt{1 - j\zeta} \tag{166}$$

$$\eta = \frac{\eta_0}{\sqrt{\tilde{\varepsilon}'}}\frac{1}{\sqrt{1 - j\zeta}} \tag{167}$$

$$v_p = \frac{c}{\sqrt{\tilde{\varepsilon}'}}\frac{1}{\sqrt{1 - j\zeta}} \tag{168}$$

$$n = \sqrt{\tilde{\varepsilon}'}\sqrt{1 - j\zeta}. \tag{169}$$

---

[25] All non-ferromagnetic materials exhibit $\tilde{\mu} = 1$. This is the case for most planetary bodies in the solar system.

[26] The loss tangent reported in the literature is directly equal to ζ, and the inverse tangent operation need not be applied.

Finally, ζ is also used to classify lossy materials. Indeed, if $\zeta < 10^{-2}$, the material is considered a low-loss dielectric, while materials with $10^{-2} \leq \zeta \leq 10^{2}$ are considered quasi-conductors and materials with $\zeta > 10^{2}$ are classified as good conductors. Furthermore, the values of α, β, k, η, v_p, and n can be approximated by taking advantage of the following approximations:

- For low-loss materials, $\zeta \ll 1$ and therefore $\sqrt{1 \pm jx} \approx 1 \pm j\frac{x}{2}$ and $\frac{1}{\sqrt{1 \pm jx}} \approx 1 \mp j\frac{\delta}{2}$.
- For good conductors, $\zeta \gg 1$ and therefore $\sqrt{1 \pm jx} \approx \sqrt{\frac{x}{2}}(1-j)$ and $\frac{1}{\sqrt{1 \pm jx}} \approx \frac{1 \mp j}{\sqrt{2\delta}}$.

This results in the characteristic parameters of dielectric non-ferromagnetic materials provided in Table 2.

Table 2. Dielectric Properties of Materials

	Free Space	Lossless Medium	Lossy Material		
			Low-loss	Quasi-conductor	Good conductor
ζ	0	0	$< 10^{-2}$	$10^{-2} \leq \zeta \leq 10^{2}$	$> 10^{2}$
α	0	0	$\frac{\pi}{\lambda}\frac{\tilde{\varepsilon}'' + \tilde{\sigma}/\omega}{\tilde{\varepsilon}'}$	$\frac{2\pi}{\lambda}\sqrt{\frac{\tilde{\varepsilon}'}{2}\left(-1+\sqrt{1+\zeta^2}\right)}$	$\frac{\pi}{\lambda}\sqrt{2\left(\tilde{\varepsilon}'' + \frac{\tilde{\sigma}}{\omega}\right)}$
β	$\frac{2\pi}{\lambda}$	$\frac{2\pi}{\lambda}\sqrt{\tilde{\varepsilon}'}$	$\frac{2\pi}{\lambda}\sqrt{\tilde{\varepsilon}'}$	$\frac{2\pi}{\lambda}\sqrt{\frac{\tilde{\varepsilon}'}{2}\left(+1+\sqrt{1+\zeta^2}\right)}$	$\frac{\pi}{\lambda}\sqrt{2\left(\tilde{\varepsilon}'' + \frac{\tilde{\sigma}}{\omega}\right)}$
n	1	$\sqrt{\tilde{\varepsilon}'}$	$\sqrt{\tilde{\varepsilon}'}\left(1 - j\frac{\zeta}{2}\right)$	$\sqrt{\tilde{\varepsilon}'}\sqrt{1-j\zeta}$	$\sqrt{\tilde{\varepsilon}'}\sqrt{\frac{\zeta}{2}}(1-j)$
k	$\frac{2\pi}{\lambda}$	$\frac{2\pi}{\lambda}n$	$\frac{2\pi}{\lambda}n$	$\frac{2\pi}{\lambda}n$	$\frac{2\pi}{\lambda}n$
η	η_0	$\frac{\eta_0}{n}$	$\frac{\eta_0}{\sqrt{\tilde{\varepsilon}'}}\left(1 + j\frac{\zeta}{2}\right)$	$\frac{\eta_0}{n}$	$\frac{\eta_0}{\sqrt{\tilde{\varepsilon}'}}\frac{1+j}{\sqrt{2\zeta}}$
v_p	c	$\frac{c}{n}$	$\frac{c}{\sqrt{\tilde{\varepsilon}'}}\left(1 + j\frac{\zeta}{2}\right)$	$\frac{c}{n}$	$\frac{c}{\sqrt{\tilde{\varepsilon}'}}\frac{1+j}{\sqrt{2\zeta}}$

III. GO Approximation Conditions at Grazing Angles

In this appendix, we show that under the GO approximation and at grazing angles, the traditional assumption that $(q_z s)^2 \gg 1$ is in general valid except for very small values of surface roughness. To do so, we first evaluate the following limit:

$$\lim_{\substack{\lambda \to 0 \\ \theta_i, \theta_s \to 90}} \frac{4\pi^2}{\lambda^2}(\cos\theta_i + \cos\theta_s)^2 s^2. \tag{170}$$

To do so, we assume s to be finite, and we assume that incident and reflected polar angles are the same. In this case, this limit can be rewritten as

$$4\pi^2 s^2 \lim_{t \to 0} \frac{(2\cos\left(\frac{\pi}{2} - t\right))^2}{t^2}. \tag{171}$$

Taylor expanding the numerator yields

$$16\pi^2 s^2 \lim_{t\to 0} \frac{t^2 + \mathcal{O}(t^4)}{t^2} = 16\pi^2 s^2. \tag{172}$$

Note that the value $16\pi^2 s^2$ is adimensional. Also, Ulaby et al. argue in [4] that the GO approximation can only be used if $(q_z s)^2 > 10$. Therefore, rearranging terms, we get that for the GO to be valid

$$s > \frac{\sqrt{10}}{4\pi} \approx 0.25\text{m}. \tag{173}$$

However, if we assume λ to be finite, then $(q_z s)^2$ tends to

$$(q_z s)^2 = 16\pi^2 \frac{s^2}{\lambda^2}\theta^2, \tag{174}$$

so the GO approximation will be valid as long as

$$s > \frac{\sqrt{10}}{4\pi\psi}\lambda \approx \frac{\lambda}{4\psi}, \tag{175}$$

where $\psi = 90 - \theta$ is the grazing angle. Also, if we do not assume θ_i and θ_s to be equal, then the condition simply becomes

$$s > \frac{\sqrt{10}}{2\pi(\psi_i + \psi_s)}\lambda \approx \frac{\lambda}{2(\psi_i + \psi_s)}. \tag{176}$$

Finally, it is common to express the condition of validity of the GO with respect to the normalized parameter ks. In that case, the GO is valid if

$$ks > \frac{\sqrt{10}}{\psi_i + \psi_s} \approx \frac{3.16}{\psi_i + \psi_s} \tag{177}$$

or, equivalently,

$$ks > \frac{1.58}{\psi} \tag{178}$$

if we assume $\psi_i = \psi_s$.

IV. Conditions of Specular Reflection under the GO Approximation

In this appendix, we prove that under the GO approximation, the normal of the points that specularly reflect power towards a receiver in any given facet is equal to

$$\hat{\boldsymbol{n}}_{GO} = \frac{\hat{\boldsymbol{k}}_s - \hat{\boldsymbol{k}}_i}{\left|\hat{\boldsymbol{k}}_s - \hat{\boldsymbol{k}}_i\right|}, \tag{179}$$

where $\hat{\boldsymbol{k}}_i$ and $\hat{\boldsymbol{k}}_s$ represent the incident and reflected unit vectors. To that end, we first state the conditions of specular reflection:

1. The polar angle of incidence θ_i must be equal to the polar angle of reflection θ_s.

2. The normal $\hat{\boldsymbol{n}}_{GO}$ must lie in the plane formed by the incident and reflected rays. Or, equivalently, the azimuthal angle of incidence and reflection, denoted ϕ_i and ϕ_s, respectively, satisfy $|\phi_s - \phi_i| = 180°$.

To prove both conditions, we consider, without loss of generality, the geometry of Figure 12. In this case, the angles θ_i and θ_s can be calculated as

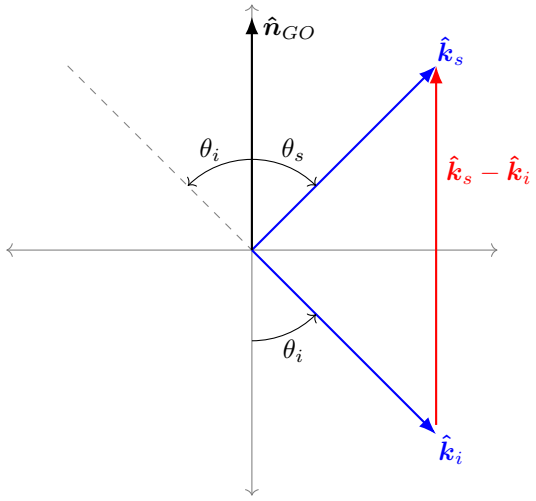

Figure 12. Specular Reflection CRS (length of vectors not to scale)

$$\theta_i = \arccos\left(\hat{\boldsymbol{k}}_i \cdot -\hat{\boldsymbol{n}}_{GO}\right) = \arccos\left(\frac{\hat{\boldsymbol{k}}_i \cdot \left(\hat{\boldsymbol{k}}_i - \hat{\boldsymbol{k}}_s\right)}{\left|\hat{\boldsymbol{k}}_s - \hat{\boldsymbol{k}}_i\right|}\right) = \arccos\left(\frac{1 - \hat{\boldsymbol{k}}_i \cdot \hat{\boldsymbol{k}}_s}{\left|\hat{\boldsymbol{k}}_s - \hat{\boldsymbol{k}}_i\right|}\right), \tag{180}$$

$$\theta_s = \arccos\left(\hat{\boldsymbol{k}}_s \cdot +\hat{\boldsymbol{n}}_{GO}\right) = \arccos\left(\frac{\hat{\boldsymbol{k}}_s \cdot \left(\hat{\boldsymbol{k}}_s - \hat{\boldsymbol{k}}_i\right)}{\left|\hat{\boldsymbol{k}}_s - \hat{\boldsymbol{k}}_i\right|}\right) = \arccos\left(\frac{1 - \hat{\boldsymbol{k}}_s \cdot \hat{\boldsymbol{k}}_i}{\left|\hat{\boldsymbol{k}}_s - \hat{\boldsymbol{k}}_i\right|}\right), \tag{181}$$

which are equal to each other because the dot product is commutative. Similarly, $\hat{\boldsymbol{k}}_i$, $\hat{\boldsymbol{k}}_s$, and $\hat{\boldsymbol{n}}_{GO}$ will lie in a plane if $\hat{\boldsymbol{k}}_i$ is perpendicular to the cross product of $\hat{\boldsymbol{k}}_s$ and $\hat{\boldsymbol{n}}_{GO}$. In other words,

$$\hat{\boldsymbol{k}}_i \cdot \left(\hat{\boldsymbol{k}}_s \times \hat{\boldsymbol{n}}_{GO}\right) = 0. \tag{182}$$

This condition is easy to prove by first noting that it can be interpreted as the triple scalar product in its determinant form:

$$\hat{\boldsymbol{k}}_i \cdot \left(\hat{\boldsymbol{k}}_s \times \hat{\boldsymbol{n}}_{GO}\right) = \det \begin{bmatrix} k_{ix} & k_{iy} & k_{iz} \\ k_{sx} & k_{sy} & k_{sz} \\ k_{sx} - k_{ix} & k_{sz} - k_{iy} & k_{sz} - k_{iz} \end{bmatrix}. \tag{183}$$

Then, we simply expand the determinant and collect terms until they all cancel out, a step obviated here for brevity.

V. The Surface Differential

This appendix provides a brief discussion of the choice of surface differential to evaluate the square of the phase integral in Equation (78). To initiate the discussion, let us recall that because the surface is random, we seek to evaluate

$$\langle |I|^2 \rangle = \langle \iint_F \iint_{F'} e^{j\boldsymbol{q}(\boldsymbol{r}-\boldsymbol{r'})} dS dS' \rangle. \tag{184}$$

Following the conventions from [4], let $Z_x = \frac{\partial z}{\partial x}$ and $Z_y = \frac{\partial z}{\partial y}$ denote the surface slopes in the x and y directions respectively, which, by definition, are also random. Then, thanks to the linearity of the expectation operator, we get

$$\langle |I|^2 \rangle = \iint_F \iint_{F'} e^{jq_x(x-x')+jq_y(y-y')} \langle \kappa \rangle dA dA', \tag{185}$$

where the random variable κ is defined as

$$\kappa = e^{jq_z(z-z')} \sqrt{Z_x^2 + Z_y^2 + 1} \sqrt{Z_{x'}^2 + Z_{y'}^2 + 1}. \tag{186}$$

Unfortunately, this quantity is difficult to evaluate analytically because it involves six stochastic Gaussian processes z, z', Z_x, Z_y, $Z_{x'}$, and $Z_{y'}$ with zero mean that are autocorrelated and, in some cases, cross correlated. To circumvent this limitation, we provide three approximations for $\langle \kappa \rangle$, two in which the slopes are assumed to not be autocorrelated, and another one where this autocorrelation is taken into account. In both cases, however, independence between the surface and the slopes is assumed to simplify the problem.

A. Approximation 1: Bound Assuming Uncorrelated Slopes

If we assume the surface and the slopes to be independent, then

$$\langle \kappa \rangle \approx \langle e^{jq_z(z-z')} \rangle \langle \sqrt{Z_x^2 + Z_y^2 + 1} \sqrt{Z_{x'}^2 + Z_{y'}^2 + 1} \rangle. \tag{187}$$

The first term $\langle e^{jq_z(z-z')} \rangle$ results in Equation (85) because it is simply the characteristic function of two correlated Gaussian variables. To evaluate the second term, we assume here that the slopes at different points of the surface are not correlated with each other. In this case,

$$\langle \sqrt{Z_x^2 + Z_y^2 + 1} \sqrt{Z_{x'}^2 + Z_{y'}^2 + 1} \rangle = \langle \sqrt{Z_x^2 + Z_y^2 + 1} \rangle \langle \sqrt{Z_{x'}^2 + Z_{y'}^2 + 1} \rangle. \tag{188}$$

Furthermore, we know that the function $f(x) = \sqrt{x}$ is concave, so we can apply Jensen's inequality to obtain

$$\langle \sqrt{Z_x^2 + Z_y^2 + 1} \rangle \leq \sqrt{\langle Z_x^2 + Z_y^2 + 1 \rangle} = \sqrt{1 - 2\rho''(0)}, \tag{189}$$

which results in

$$\langle \sqrt{Z_x^2 + Z_y^2 + 1} \sqrt{Z_{x'}^2 + Z_{y'}^2 + 1} \rangle \leq 1 - 2\rho''(0). \tag{190}$$

Therefore, and assuming a Gaussian correlation function of the form $\rho(\xi) = s^2 e^{-\xi^2/l^2}$, we get

$$\langle \kappa \rangle \approx e^{-q_z^2 s^2 (1-\rho)} \left(1 + \frac{4s^2}{l^2} \right). \tag{191}$$

B. Approximation 2: Exact Value Assuming Uncorrelated Slopes

A more exact but also more cumbersome approximation can be found by studying the distribution of $\sqrt{Z_x^2 + Z_y^2 + 1}$. In particular, we note that

$$\left(\frac{Z_x}{s_z}\right)^2 + \left(\frac{Z_y}{s_z}\right)^2 \sim \chi_2^2, \tag{192}$$

where χ_2^2 denotes the Chi-square distribution with two degrees of freedom and s_z denotes the standard deviation of the slopes, which can be shown to be equal to [27]

$$s_z^2 = -s^2\rho''(0). \tag{193}$$

Therefore, the random variable $Q = 1 + Z_x^2 + Z_y^2$ has a probability density function of the form

$$f_Q(q) = \frac{1}{2s_z^2} e^{\frac{q-1}{2s_z^2}}, \tag{194}$$

and $P = \sqrt{Q}$ is distributed as

$$f_P(p) = f_Q(q)\left|\frac{\partial Q}{\partial P}\right| = \frac{|p|}{s_z^2} e^{-\frac{p-1}{2s_z^2}}. \tag{195}$$

Note that both Q and P have support $[1, \infty)$ so that

$$\langle\sqrt{Z_x^2 + Z_y^2 + 1}\rangle = \int_1^\infty p f_P(p) dp = 1 + \sqrt{\frac{\pi}{2}}\left(1 - \operatorname{erf}\left(\frac{1}{\sqrt{2}s_z}\right)\right) s_z e^{\frac{1}{2s_z^2}}. \tag{196}$$

Consequently, if the terrain correlation function is Gaussian, then

$$s_z^2 = 2\frac{s^2}{l^2} \tag{197}$$

and

$$\langle\kappa\rangle = e^{-q_z^2 s^2(1-\rho)}\left[1 + \sqrt{\pi}\left(1 - \operatorname{erf}\left(\frac{l}{2s}\right)\right)\frac{s}{l} e^{\frac{l^2}{4s^2}}\right]^2. \tag{198}$$

C. Approximation 3: Bound Assuming Autocorrelated Slopes

We once again assume independence between the surface and its slopes so that

$$\langle\kappa\rangle \approx \langle e^{jq_z(z-z')}\rangle\langle\sqrt{Z_x^2 + Z_y^2 + 1}\sqrt{Z_{x'}^2 + Z_{y'}^2 + 1}\rangle. \tag{199}$$

Furthermore, the surface slope term can be expanded to yield

$$\langle\sqrt{(Z_x^2 + Z_y^2 + 1)(Z_{x'}^2 + Z_{y'}^2 + 1)}\rangle \leq \sqrt{\langle 1 + Z_x^2 + Z_y^2 + Z_x^2 Z_{x'}^2 + Z_y^2 Z_{y'}^2 + Z_y^2 Z_{x'}^2 + Z_x^2 Z_{y'}^2\rangle}, \tag{200}$$

which, upon assuming that the terrain has isotropic roughness properties in the x and y directions, simplifies to

$$\langle\sqrt{(Z_x^2 + Z_y^2 + 1)(Z_{x'}^2 + Z_{y'}^2 + 1)}\rangle \leq \sqrt{1 + 2\left[\langle Z_x^2\rangle + \langle Z_x^2 Z_{x'}^2\rangle + \langle Z_x^2 Z_{y'}^2\rangle\right]}. \tag{201}$$

Next we evaluate the three expectations in this last expression, which leads to

$$\langle Z_x^2 \rangle = -\rho''(0) \tag{202}$$

$$\langle Z_x^2 Z_{x'}^2 \rangle = 2\rho''(\xi)^2 + \rho''(0)^2 \leq 3\rho''(0)^2 \tag{203}$$

$$\langle Z_x^2 Z_{y'}^2 \rangle = \rho''(0)^2. \tag{204}$$

The proofs for each term are provided in the subsection following this discussion. Consequently,

$$\langle \kappa \rangle \approx e^{-q_z^2 s^2 (1-\rho)} \sqrt{1 + 2\left[-\rho''(0) + 3\rho''(0)^2 + \rho''(0)^2\right]} \tag{205}$$

which, when evaluated for a Gaussian correlation function, yields

$$\langle \kappa \rangle \approx e^{-q_z^2 s^2 (1-\rho)} \sqrt{1 + 4\frac{s^2}{l^2} + 32\frac{s^4}{l^4}}. \tag{206}$$

D. Comparison of Approximations

Figure 13 plots approximations (191), (198), and (206) normalized as follows:

$$\langle \hat{\kappa} \rangle = \frac{\langle \kappa \rangle}{e^{-q_z^2 s^2 (1-\rho)}} \tag{207}$$

It can be observed that for small values of s/l, the three approximations essentially yield the same result. However, as s/l increases, the effects of cross-correlations between surface slopes becomes increasingly noticeable.

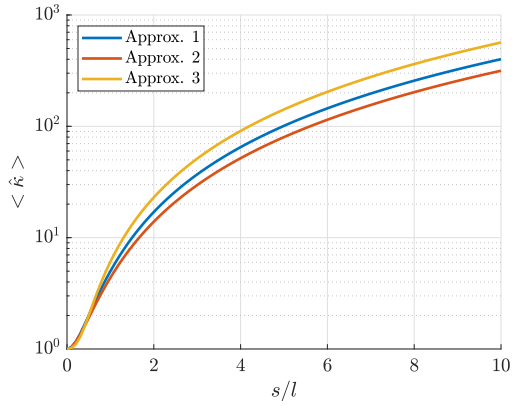

Figure 13. Comparison of Approximations

E. Moments of the Surface Slopes

In this subsection, we derive basic statistical properties of the surface slopes. To start, recall here that we have assumed the terrain $z(x, y)$ to be modeled as a two-dimensional Gaussian process with zero mean and autocorrelation function $\rho(x - x', y - y') = \rho(\xi)$. Because the surface slopes are defined by means of derivatives,

it is appropriate to recall basic properties for the derivative operator when applied to a stochastic process, namely [27]:

- The derivative of a Gaussian stochastic process is also a Gaussian stochastic process.
- $\langle Z_x \rangle = \frac{\partial}{\partial x}\langle z(x,y) \rangle$ and $\langle Z_y \rangle = \frac{\partial}{\partial y}\langle z(x,y) \rangle$
- Z_x is autocorrelated with $\rho_{Z_x}(\xi) = -\frac{\partial^2}{\partial \xi^2}\rho(\xi) = \rho''(\xi)$. The same result applies to Z_y.
- If Z_x and $Z_{x'}$ are jointly Gaussian distributed with zero mean and covariance $\rho_{Z_x}(\xi)$, then the covariance of Z_x^2 and $Z_{x'}^2$ is equal to $2\rho_{Z_x}^2(\xi)$. The same result also applies to Z_y and $Z_{y'}$.

Using these facts, it is immediate to see that $\langle Z_x^2 \rangle = \langle Z_y^2 \rangle = -\rho''(0)$ and therefore

$$\langle Z_x^2 Z_{x'}^2 \rangle = \mathrm{Cov}\left(Z_x^2, Z_{x'}^2\right) + \langle Z_x^2 \rangle \langle Z_{x'}^2 \rangle = 2\rho''(\xi)^2 + \rho''(0)^2. \tag{208}$$

Also, to calculate $\langle Z_x^2 Z_{y'}^2 \rangle$, we start by showing that $\langle Z_x Z_{y'} \rangle$ are uncorrelated. In particular,

$$\begin{aligned} \langle Z_x Z_{y'} \rangle &= \lim_{\substack{\Delta x \to 0 \\ \Delta y' \to 0}} \langle \frac{z(x+\Delta x, y) - z(x,y)}{\Delta x} \frac{z(x', y'+\Delta y', x') - z(x', y')}{\Delta y'} \rangle \\ &= \lim_{\substack{\Delta x \to 0 \\ \Delta y' \to 0}} \frac{\rho(x+\Delta x - x', y - y' - \Delta y') + \rho(x - x', y - y')}{\Delta x \Delta y'} - \\ &\quad \lim_{\substack{\Delta x \to 0 \\ \Delta y' \to 0}} \frac{\rho(x+\Delta x - x', y - y') + \rho(x - x', y - y' - \Delta y')}{\Delta x \Delta y'}. \end{aligned} \tag{209}$$

Next, we assume that the autocorrelation function is Gaussian and calculate its Taylor expansion around the origin. This results in

$$\rho(u,v) \approx s^2 \left(1 - \frac{u^2 + v^2}{l^2}\right). \tag{210}$$

Substituting Equation (210) into Equation (209) and carrying out the necessary summations results in the numerator of Equation (209) being equal to zero. Therefore, we have shown that

$$\langle Z_x Z_{y'} \rangle = 0. \tag{211}$$

Finally, because $\langle Z_x \rangle = \langle Z_{y'} \rangle = 0$, we have that

$$\langle Z_x Z_{y'} \rangle = \mathrm{Cov}(Z_x, Z_{y'}) = 0 \tag{212}$$

and, consequently, $\mathrm{Cov}(Z_x^2, Z_{y'}^2) = 0$. This yields the final result:

$$\langle Z_x^2 Z_{y'}^2 \rangle = 0 + \langle Z_x^2 \rangle \langle Z_{y'}^2 \rangle = \rho''(0)^2. \tag{213}$$

VI. RCS of Horizontal Square Facet

In this appendix, we specialize the results from Section IV.A.10 to a square facet because it is most common in the literature — see, for instance, [4, 7, 28]. Figure 14 shows a single square facet of side $2L$ in isolation with its positively oriented contour.

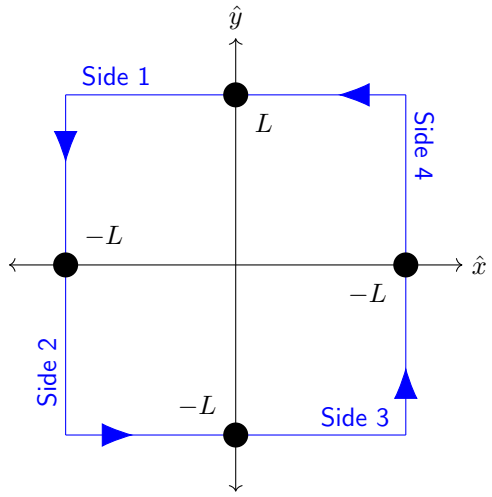

Figure 14. Square Facet

The coordinates of its vertices are (L, L), $(-L, L)$, $(-L, -L)$, and $(L, -L)$. Therefore, upon substituting these values into Equations (112) and (113), we obtain:

$$\alpha_1 = q_x \frac{L-L}{2} + q_y \frac{-L-L}{2} = -q_y L \tag{214}$$

$$\alpha_2 = q_x \frac{L+L}{2} + q_y \frac{L-L}{2} = +q_x L \tag{215}$$

$$\alpha_3 = q_x \frac{-L+L}{2} + q_y \frac{L+L}{2} = +q_y L \tag{216}$$

$$\alpha_4 = q_x \frac{-L-L}{2} + q_y \frac{-L+L}{2} = -q_x L \tag{217}$$

and

$$\beta_1 = q_x \frac{L+L}{2} + q_y \frac{-L+L}{2} = +q_x L \tag{218}$$

$$\beta_2 = q_x \frac{L-L}{2} + q_y \frac{L+L}{2} = +q_y L \tag{219}$$

$$\beta_3 = q_x \frac{-L-L}{2} + q_y \frac{L-L}{2} = -q_x L \tag{220}$$

$$\beta_4 = q_x \frac{-L+L}{2} + q_y \frac{-L-L}{2} = -q_y L. \tag{221}$$

Furthermore,

$$\Delta x_1 = -\Delta x_3 = 2L \tag{222}$$

$$\Delta x_2 = \Delta x_4 = 0 \tag{223}$$

and

$$\Delta y_1 = \ \Delta y_3 = \ 0 \tag{224}$$

$$\Delta y_2 = -\Delta y_4 = 2L. \tag{225}$$

Upon substituting these values into Equation (116) and using the fact that the sinc function is even, we get

$$\begin{aligned} I_0 =& \frac{(2L)^2}{|q_x - q_y|^2} \left| \mathrm{sinc}\left(q_x L\right) \left(e^{-jq_y L} - e^{jq_y L}\right) + \mathrm{sinc}\left(q_y L\right) \left(e^{jq_x L} - e^{-jq_x L}\right) \right|^2 \\ =& \frac{(2L)^2}{|q_x - q_y|^2} \left|2j\right|^2 \left| -\mathrm{sinc}\left(q_x L\right) \sin\left(q_y L\right) + \mathrm{sinc}\left(q_y L\right) \sin\left(q_x L\right) \right|^2 \\ =& \frac{2^2(2L)^2}{|q_x - q_y|^2} \left| -(q_y L)\mathrm{sinc}\left(q_x L\right) \mathrm{sinc}\left(q_y L\right) + (q_x L)\mathrm{sinc}\left(q_y L\right) \mathrm{sinc}\left(q_x L\right) \right|^2 \\ =& \frac{(2L)^4}{|q_x - q_y|^2} \left|q_x - q_y\right|^2 \mathrm{sinc}^2\left(q_x L\right) \mathrm{sinc}^2\left(q_y L\right) \\ =& (2L)^4 \mathrm{sinc}^2\left(q_x L\right) \mathrm{sinc}^2\left(q_y L\right). \end{aligned} \tag{226}$$

Finally, we note that $A_{\mathrm{facet}} = (2L)^2$, which results in

$$\sigma_{\mathrm{coh}} = \left(1 + \frac{4s^2}{l^2}\right) \frac{k^2}{4\pi} e^{-(q_z s)^2} Z A_{\mathrm{facet}}^2 \mathrm{sinc}^2\left(q_x L\right) \mathrm{sinc}^2\left(q_y L\right). \tag{227}$$

Observe that the obtained solution agrees with previous solutions found using the PO model. Indeed, in appendix 12D of [4], Ulaby et al. show that the coherent scattering RCS of a square surface is proportional to

$$I_{00} = \left|a_0\right|^2 e^{-(q_z s)^2} A_{\mathrm{facet}}^2 \mathrm{sinc}^2\left(q_x L\right) \mathrm{sinc}^2\left(q_y L\right), \tag{228}$$

where $\left|a_0\right|^2$ is a constant parameter that differs from our derived value because of differences between the GO and PO approximations.